Spectrin condensates provide a nidus for assembling the axonal membrane-associated periodic skeleton

Nicholas P Boyer, Rohan Sharma, Theresa Wiesner, Christopher Parperis, Antoine Delamare, Florence Pelletier, Nicolas Jullien, Anshul M Bhatt, Leonardo A Parra-Rivas, Patrick J Kearney, et al.

To cite this version:

Nicholas P Boyer, Rohan Sharma, Theresa Wiesner, Christopher Parperis, Antoine Delamare, et al.. Spectrin condensates provide a nidus for assembling the axonal membrane-associated periodic skeleton. iScience, 2026, 29, ⟨10.1016/j.isci.2025.114454⟩. ⟨hal-05489614⟩

HAL Id: hal-05489614
https://amu.hal.science/hal-05489614v1

Submitted on 2 Feb 2026

iScience

Article

Spectrin condensates provide a nidus for assembling the axonal membrane-associated periodic skeleton

Graphical abstract

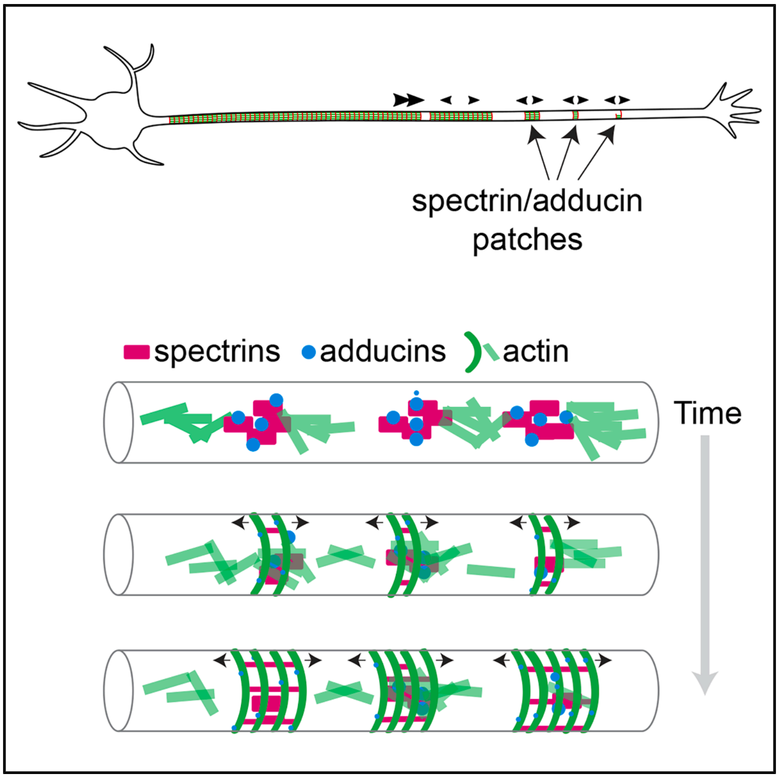

Highlights

- Events leading to membrane-periodic skeleton (MPS) assembly in axons are unclear
- Patches of MPS components, spectrin/adducin, in distal axons behave like condensates
- Stretch of spectrin-repeats triggers condensates and provide nidus for MPS assembly
- Actin incorporation into spectrin/adducin patches generate ultimate stable MPS

Authors

Nicholas P. Boyer, Rohan Sharma, Theresa Wiesner, ..., Farbod Shavarebi, Christophe Leterrier, Subhojit Roy

Correspondence

rosharma@health.ucsd.edu (R.S.),
christophe.leterrier@univ-amu.fr (C.L.),
sroy@ucsd.edu (S.R.)

In brief

Neuroscience; Molecular neuroscience; Cell biology

Boyer et al., 2026, iScience *29*, 114454
January 16, 2026 © 2025 The Author(s). Published by Elsevier Inc.
https://doi.org/10.1016/j.isci.2025.114454

iScience

CellPress
OPEN ACCESS

Article

Spectrin condensates provide a nidus for assembling the axonal membrane-associated periodic skeleton

Nicholas P. Boyer,[1,4] Rohan Sharma,[1,4,*] Theresa Wiesner,[2] Christopher Parperis,[2] Antoine Delamare,[2] Florence Pelletier,[2] Nicolas Jullien,[2] Anshul M. Bhatt,[1] Leonardo A. Parra-Rivas,[1] Patrick J. Kearney,[1] Farbod Shavarebi,[1] Christophe Leterrier,[2,*] and Subhojit Roy[1,3,5,*]
[1]Department of Pathology, University of California, San Diego, 9500 Gilman Drive, La Jolla, CA, USA
[2]Aix Marseille Université, CNRS, INP UMR7051, NeuroCyto, 13005 Marseille, France
[3]Department of Neurosciences, University of California, San Diego, 9500 Gilman Drive, La Jolla, CA, USA
[4]These authors contributed equally
[5]Lead contact
*Correspondence: rosharma@health.ucsd.edu (R.S.), christophe.leterrier@univ-amu.fr (C.L.), sroy@ucsd.edu (S.R.)
https://doi.org/10.1016/j.isci.2025.114454

SUMMARY

In axons, α/β-spectrins, adducin, and actin filaments assemble into a lattice underneath the plasma membrane, but the mechanistic events leading to this membrane-associated periodic skeleton (MPS) are unclear. Visualizing MPS-components in developing axons, we found distal focal patches containing spectrins and adducin (but sparse actin filaments) with biophysical properties reminiscent of biomolecular condensation. Overexpressing spectrin repeats – constituents of α/β-spectrins – in heterologous cells triggered condensate formation, and preventing the association of βII-spectrin with actin filaments or membranes also facilitated condensation. Introducing a stretch of spectrin-repeats in neurons before MPS establishment triggered ectopic condensate-like structures in the soma and disrupted the axonal lattice, advocating a functional role for biomolecular condensation. We propose a condensation-assembly model where spectrin-repeats trigger focal phase separated condensates, providing a nidus for MPS assembly that recruits actin filaments to ultimately generate the stable lattice. Our overall model is supported by recent studies showing phase-separation via coiled-coil domains and recruitment/polymerization of actin by other condensate-forming proteins.

INTRODUCTION

Super-resolution microscopy revealed a subplasmalemmal cytoskeletal lattice in axons, composed of α/β-spectrins, adducin, actin, and other associated proteins.[1] The axonal MPS is thought to be a stable meshwork with parallel arrays of actin filaments spaced at∼190 nm by spanning spectrin tetramers – cytoskeletal integrators composed of α/β-spectrins. Recent studies suggest that actin within the MPS may be organized as "braids" twisting along the shaft of the axon.[2–4] The MPS has been seen in axons from a variety of species,[5] as well as in living neurons[6,7] and brain slices.[1,6] Several functions have been attributed to the MPS, such as conferring structural stability to the axon,[8–10] acting as a scaffold for organizing signaling complexes,[11,12] and regulating axonal diameters.[13,14]

While substantial progress has been made in identifying component parts of the MPS, mechanistic events leading to the formation of these intricate structures are less clear. A unique aspect of axonal MPS development, compared to other cytoskeletal structures in somatodendritic domains, is that the local availability of the constituent proteins along the axon-shaft would depends on axonal transport from distant cell bodies. Key constituents of the MPS, such as spectrin, adducin, and actin, are known to move in slow axonal transport,[15–20] putting constraints on the availability of building blocks for assembly. How are all the necessary components for assembling the periodic lattice readily available in the axon shaft – particularly during periods of axonal growth – and how does the complex structure arise from these building blocks? Contrasting models have been proposed to explain the origin of the axonal MPS. A "propagation model" was proposed, where the MPS first emerges in the proximal axon adjacent to the cell body, followed by the distal propagation of the lattice structure.[21] However, there is no direct evidence for this model, and no precedence for such templated proximal to distal assembly along the axon. Another study reported focal patches of spectrin in distal axon shafts of developing neurons,[22] proposing a different model where the MPS originates from the base of growth cones, with distal spectrin patches coalescing over time to form a continuous periodic structure. However, these conclusions were drawn from a limited number of time-points, and there is no evidence for coalescence of spectrin patches. Similar spectrin patches were also recently reported in axons of human iPSC-neurons.[23]

Revisiting the issue, we systematically visualized MPS components in cultured hippocampal neurons as they develop. We confirmed the observation that the MPS in the most proximal part of axons was established early, and that focal patches of spectrins are present in distal growing axons. Examining these patches, we saw that they contained α/β-spectrins and adducin, but scant filamentous actin (F-actin). Collectively, our experiments in non-neuronal cells and neurons support the view that these distal spectrin/adducin patches are biomolecular-condensates – driven by the phase separation of spectrin-repeats – that recruit actin filaments to ultimately form the mature MPS. In our model, spectrin condensates act as depots for storing the building blocks necessary for MPS assembly, suggesting a role for phase separation in this process. A discontinuous MPS may also allow for axonal plasticity and homeostasis, and we speculate that such mechanisms may play a wider role in assembling cytoskeletal structures in other contexts.

RESULTS

Distal axons contain patches of spectrins and adducin that have sparse actin filaments

We first visualized the distribution of key MPS proteins – spectrins, adducin, and actin – in developing axons of mouse cultured hippocampal neurons fixed between 2 and 10 days *in vitro* (DIV, Figure 1A). Cultured hippocampal neurons develop in a stereotypical manner, with multiple tapering dendrites and a single elongated axon (Figure 1B). The staining pattern of spectrins and adducin over time is shown in Figures 1C–1E at early developmental stages (2 DIV), spectrins and adducin were concentrated in the proximal axon – defined here as the proximal third of its total length – around the presumptive axon initial segment (AIS, yellow bracket), with the staining tapering off distally (Figure 1C). However, by 7 DIV, small, isolated patches of spectrin and adducin began to appear along distal axons, defined here as the distal third of its total length (Figures 1D and 1E). Such spectrin/adducin patches were a common feature at DIV 7, essentially seen in all axons (see Figure S1A). The patches contained small particles of spectrin/adducin, and became more frequent and brighter as axons developed. The distribution of other membranous organelles did not meaningfully overlap with spectrin patches (Figures S1B–S1D). Patches and gaps measured ∼3.76 ± 0.12 μm and 2.64 ± 0.14 μm, respectively, and both density and size of patches decreased distally along the length of the axon (Figure 1F; mean ± SEM, gaps/patches were analyzed from a sample of 9 axons from 9 DIV neurons). To determine the quantitative distribution of these patches, we designed an algorithm to measure staining discontinuities (Figure 1G, "discontinuity factor" δ – see STAR Methods for details). Briefly, δ is more positive in regions with distinct patches of fluorescence, and more negative in homogenous regions. Measuring δ along axons from the soma to the growth cone, we found that patches formed by αII/βII-spectrin and adducin were consistently pronounced in distal axons, whereas βIII-tubulin (morphologic marker) was smoother throughout (Figure 1H). Note that in general, the distal patchiness of spectrins/adducin in the axon is more pronounced at later developmental stages. Though it was technically difficult to evaluate patchiness in older, dense cultures, spectrin can also have a patch-like distribution in more mature axons – particularly in segments that are distant from synapses (Figure S2) – suggesting that these patches may have additional roles beyond development.

Previous studies have shown that the disruption of actin also disrupted MPS periodicity, suggesting a role of actin in MPS-assembly.[21] Unlike spectrin/adducin that were seen within single patches (see Figure 1D), we noticed that filamentous actin (F-actin) was not consistently present in these focal accumulations. To characterize the distribution of axonal actin, we fixed and stained neurons for αII/βII-spectrin, F-actin, and monomeric actin (G-actin), using βIII-tubulin staining as a morphological marker. As shown in Figures 2A and 2B, the distribution of F-actin was discontinuous along the axon shaft, and distal spectrin patches often lacked F-actin. Quantitative analysis showed that significantly less F-actin was associated with spectrin in distal axons (Figure 2C, also see Figures S3A–S3C). A similar staining-pattern was also seen with an actin-nanobody (Figure S3D). We also examined the nanostructure of these patches using stochastic optical reconstruction microscopy (STORM), at a timepoint when the spectrin/adducin patches are clearly visible (6 DIV). As expected, proximal axons had a continuous periodic spectrin lattice with ∼190 nm periodicity; however, this structured organization was lost in distal axons, and imaging of patches revealed incomplete lattices and globular structures (Figure 2D, also see Figure S3E). Unlike proximal axons, actin was not co-organized with spectrin in distal regions (Figure 2E). Taken together, the data suggest that while the distal axonal patches are enriched in spectrins and adducin, they are often devoid of actin filaments, suggesting that the absence of F-actin may favor the assembly of these patches (also see βII-spectrin/actin data later). Small puncta of spectrin were dispersed in axonal growth cones, and there was partial colocalization with actin (Figure S3F).

Spectrin patches in distal axons show condensate-like behavior

The morphology of spectrin/adducin patches in distal axons is reminiscent of membrane-less organelles or biomolecular condensates, which can range from small nanoclusters to "mesoscopic" protein condensates that are several hundred nanometers in size.[24–27] Specific to spectrin, previous studies in non-neuronal cells have shown that in response to DNA damage, nuclear αII-spectrin redistributes into bright foci resembling biomolecular condensates.[28] Components of biomolecular condensates can remain stably concentrated within a structure for long periods of time, but a cardinal feature is that molecules within such structures exchange with the surrounding cytoplasm within timescales of seconds to minutes.[29,30] To test if the axonal spectrin patches also behave in this manner, we performed fluorescence recovery after photo bleaching (FRAP) experiments in cultured neurons (Figure 3A). Neurons were transfected with low levels of αII-spectrin tagged to monomeric Green-Lantern (mGL), and the low expressors were selected for analyses (see STAR Methods for details). While fluorescence was continuous in proximal regions, discrete patches of αII-spectrin:mGL were seen in distal axons (Figure 3B), reminiscent of the pattern seen with endogenous αII-spectrin. These αII-spectrin:mGL patches were stable for the entire duration of imaging (15 min), and did not show any merging/splitting behaviors (Video S1). FRAP experiments showed that while there was minimal recovery of αII-spectrin:mGL fluorescence in proximal axons – consistent with

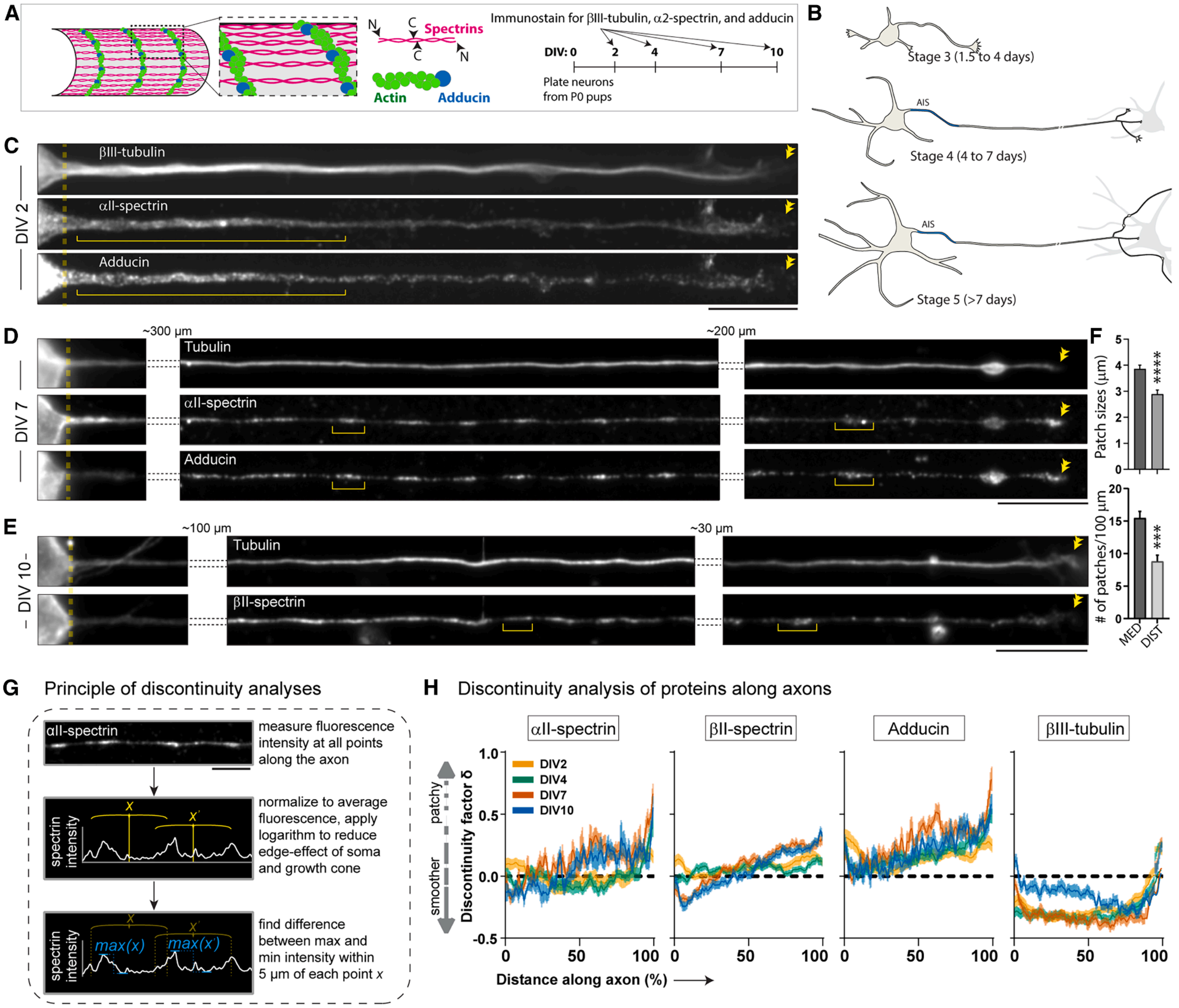

Figure 1. Spectrin/adducin patches in distal axon during development

(A) Schematic of the MPS and timing of experiments. Hippocampal neurons were obtained from P0 pups and cultured for 2, 4, 7, or 10 days *in vitro* (DIV) before fixation and immunostaining.

(B) Schematic showing the development of the axon through neuronal stages 3–5. Note formation of the axon initial segment (AIS) during stage 4 and synaptic contacts with target neurons at stage 5.

(C–E) Representative images of 2 DIV and 7 DIV neurons stained for βIII-tubulin (volume marker), αII-spectrin or βII-spectrin, and adducin. Note the accumulation of spectrin and adducin in the proximal axon. Soma/axon junction is marked by a dashed line, double arrowheads label the growth cone, and a bracket marks patches along the axon. Scale bars = 10 µm.

(F) Size and density of spectrin patches were greater in axonal segments closer to the AIS/proximal axon (mean ± SEM, unpaired t test with Welch's correction, data analyzed from a sample of 9 axons from 9 DIV neurons, ***$p < 0.0001$, ****$p < 0.00001$).

(G) Quantification of axon patches. Fluorescence intensity was measured at every point along the axon. The maximum and minimum fluorescence within 5 µm of each point was calculated, and the difference was normalized to the average fluorescence within 20 µm, giving an estimate of the discontinuity of fluorescence. The logarithm of this normalized difference was the discontinuity factor δ (see STAR Methods for more details). Scale bars = 5 µm.

(H) Discontinuity factors for αII/βII-spectrin, adducin, and βIII-tubulin in neurons fixed at 2, 4, 7, or 10 DIV. Note that a higher positive δ indicates a patchier distal axon, and in general, discontinuity in the distal axon increases as the axon develops (data from 9 to 46 cells for each time point, from 3 independent cultures).

a stable lattice (see STAR Methods, Figure S4A, and Zhong et al., 2014[21]) – fluorescence in photobleached distal αII-spectrin:mGL patches recovered partially within several minutes, indicating that cytosolic spectrin molecules from the axon shaft can exchange with the axonal patches (Figures 3C and 3D). A similar pattern was seen in FRAP experiments with βII-spectrin:GFP (Figure S4B). Studies have recognized phase separation in diverse cellular contexts, ranging from highly mobile granules that exchange rapidly with the surrounding cytosol,[31,32] to condensates that behave as solids, or have solid-like features.[33,34] Axonal

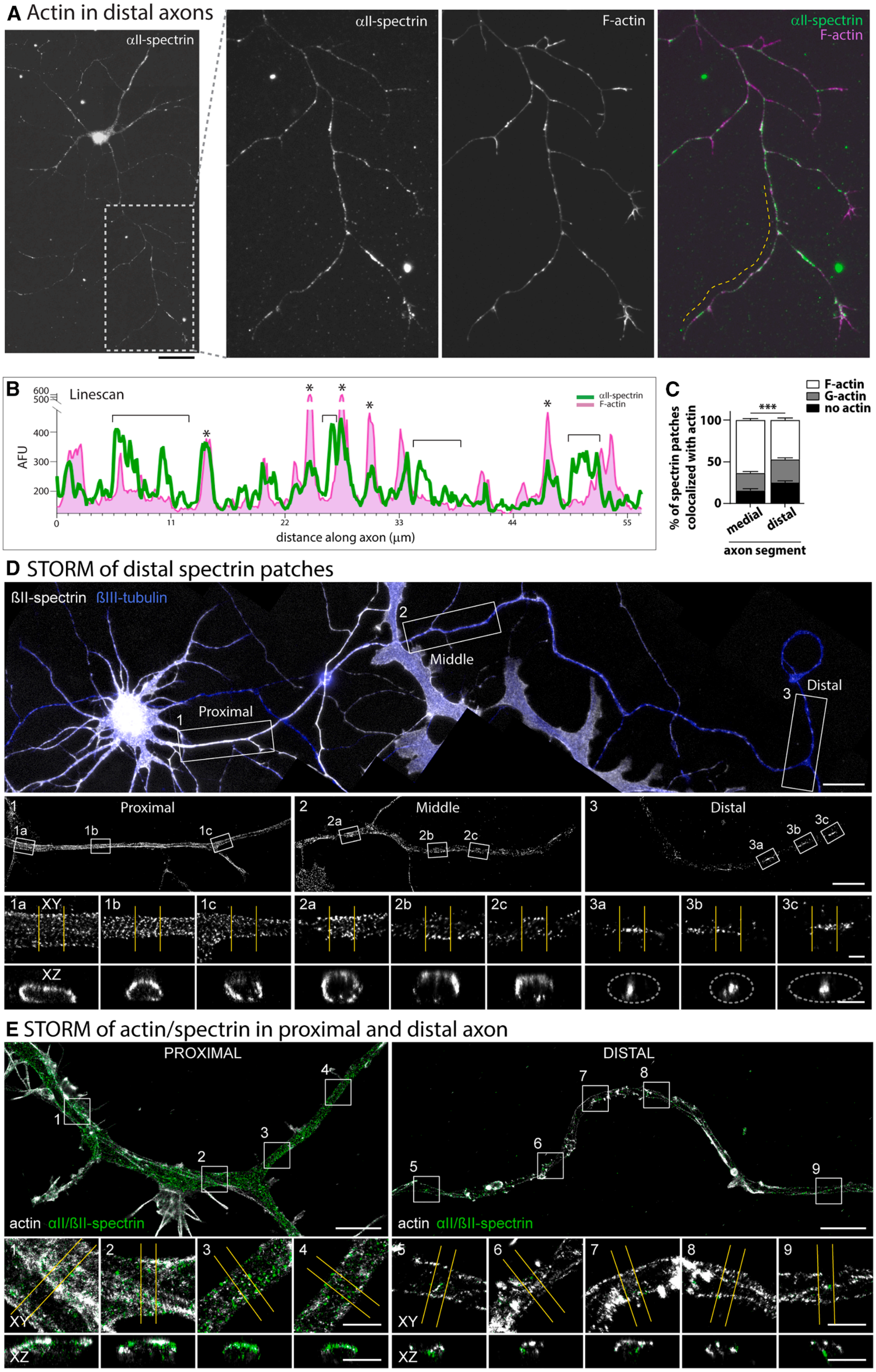

(legend on next page)

αII-spectrin:mGL patches were also resistant to aliphatic alcohols that can disrupt the low-complexity interactions that drive some forms of phase separation (Figure S4C), suggesting a more solid-like behavior, and also arguing against a model where the patches coalesce over time.

αII-spectrin can form bimolecular condensates in heterologous cells

Many previous studies have explored phase separation by overexpressing putative condensate components in heterologous cells, to facilitate molecular interactions that would promote phase separation and generate focal condensates,[35–37] though such experiments need to be interpreted with caution, and in our case, considered in parallel with findings in neurons. Toward this, we transfected HEK293T cells with mGL-tagged αII/βII-spectrins or adducin and investigated putative condensate-like behaviors (Figure 4A; also see Figure S5). The distributions of FL versions of mGL-tagged αII-spectrin, βII-spectrin, and adducin were distinct in HEK293T cells (Figure 4B). While FL-αII-spectrin formed inclusions resembling condensates, FL-βII-spectrin – that has actin-binding domains[38] – had a membranous pattern (also see Video S2), and FL-adducin had a diffuse, cytosolic distribution (Figure 4B). We noticed that cells with rounded inclusions sometimes also had large “islands” of fluorescence that were typically seen along the periphery of the cell, underneath the plasma membrane (see Figure S6 for further characterization). Other studies on phase separation have also reported similar swaths of fluorescence upon the overexpression of condensate-forming proteins.[39,40] While physical processes that control the size of condensates are not well understood,[41,42] it is known that native membrane-less assemblies such as the nucleoli have large, non-normal variations in size-distributions.[43,44] Thus, the behavior of spectrin condensates may be due to underlying biophysical processes that regulate the formation and maintenance of these assemblies, or alternatively, the large accumulations might be an effect of the association of spectrins with the subplasmalemmal F-actin network, which alters the physical nature of these condensates. As controls, we also tested a synthetic membraneless organelle engineered from intrinsically disordered arginine/glycine-rich RGG domains[31] that showed small focal inclusions in HEK293T cells, and soluble (untagged) mGL, which was diffusely distributed as expected (Figure 4C).

Live imaging of FL-αII-spectrin inclusions showed that they were stable and did not show significant merging/splitting behavior (Figure 4D and Video S3). Biomolecular condensation has two key features: 1) exchange of molecules between the condensate and surrounding cytosol; and 2) redistribution of molecules within the condensate by internal diffusion. Accordingly, we used two FRAP modalities to test if FL-αII-spectrin:mGL inclusions showed liquid-like behaviors. We first photobleached entire αII-spectrin:mGL inclusions in HEK293T cells (full-bleach) and evaluated FRAP (see schematic in Figure 4E, top). As shown in the serial snapshots from a representative example and ensemble statistics (Figure 4E, middle and bottom), fully bleached αII-spectrin inclusions recovered approximately half of their fluorescence within ∼45 s, indicating that spectrin molecules can readily move across the inclusion surface. Next, we used a recently described workflow called model-free calibrated half-FRAP (MOCHA-FRAP[33]) to evaluate the redistribution of molecules within a single αII-spectrin:mGL puncta. The principle of this quantitative assay is that bleaching half of a condensate would ensure that recovery would only occur from the unbleached half – in addition to ongoing exchange between the cytoplasm and condensate – and the authors mathematically determined that a dip-depth of fluorescence between 10 and 50% would correspond to liquid-liquid phase separation (Figure 4F – see Muzzopappa et al[33] for more details). MOCHA-FRAP analyses of FL-αII-spectrin puncta show that the fluorescence dip-depth was 19.1% on average, which falls within the predicted range for phase separation (Figure 4G, also see Figure S7A). MOCHA-FRAP analyses of RGG-GFP-RGG condensates showed a fluorescence dip-depth of 14.2%, also within the predicted range for phase separation (Figure 4H), while applying similar procedures on αII-spectrin:mGL inclusions in fixed cells did not show any change, as expected (Figures S7B and S7C).

Spectrin repeats can form biomolecular condensates in heterologous cells

Next, we examined the expression of αII-spectrin fragments in HEK293T cells Figure 5A). FL-αII-spectrin is composed of 20 spectrin repeats, which are made of canonical coiled-coil domains that are found in all members of the spectrin superfamily of cytoskeletal integrators.[45] A portion of repeat 9 is homologous to SH3 domains, and EF-hands motifs at the C-terminus are involved in modulating interactions with βII-spectrins. As expected, algorithms predicting intrinsic disorder (see STAR Methods) did not find significant disordered regions within FL-αII-spectrin (Figure S7D), consistent with the highly structured coiled-coil domains that comprise spectrin repeats. Since

Figure 2. Paucity of actin filaments in distal spectrin patches

(A) Neurons at 7 DIV were fixed and stained for F-actin and αII-spectrin. In zoomed insets of the distal axon, note that many spectrin patches lack F-actin, best seen in the merged image on the right. Scale bars = 10 μm.

(B) A maximum-intensity line-scan of the dashed yellow line from (A). Note that many patches of αII-spectrin do not coincide with peaks of F-actin (brackets), while some do (asterisks).

(C) Quantification of αII-spectrin patch colocalization with F-actin (phalloidin) or G-actin (DNase). Note that more spectrin patches in the proximal and medial thirds of the axon contained F-actin, while patches in the distal third were more likely to colocalize with G-actin or contain no actin (mean ± SEM, two-way ANOVA, data from 31 cells from 3 independent cultures, ***$p < 0.001$).

(D and E) STORM of βII-spectrin (D) or αII/βII-spectrin (mixed antibodies) together with actin (E) in proximal (1), middle (2), and distal (3) regions of a rat hippocampal neuron fixed at 6 DIV. XY zooms and XZ axis projections of the regions delineated by yellow lines are shown later in discussion, together with a 3D rendering of the section. Note that while proximal axons have the expected periodic appearance of spectrin, middle and distal axonal regions have interrupted periodicity with incomplete annular structures, or patchy distribution with no periodicity. Though most of the actin in proximal axons was aligned with spectrin as expected, this was not the case in distal axons (E). Scale bars = 20 μm (top view), 5 μm (middle views), 500 nm (zooms and transverse sections).

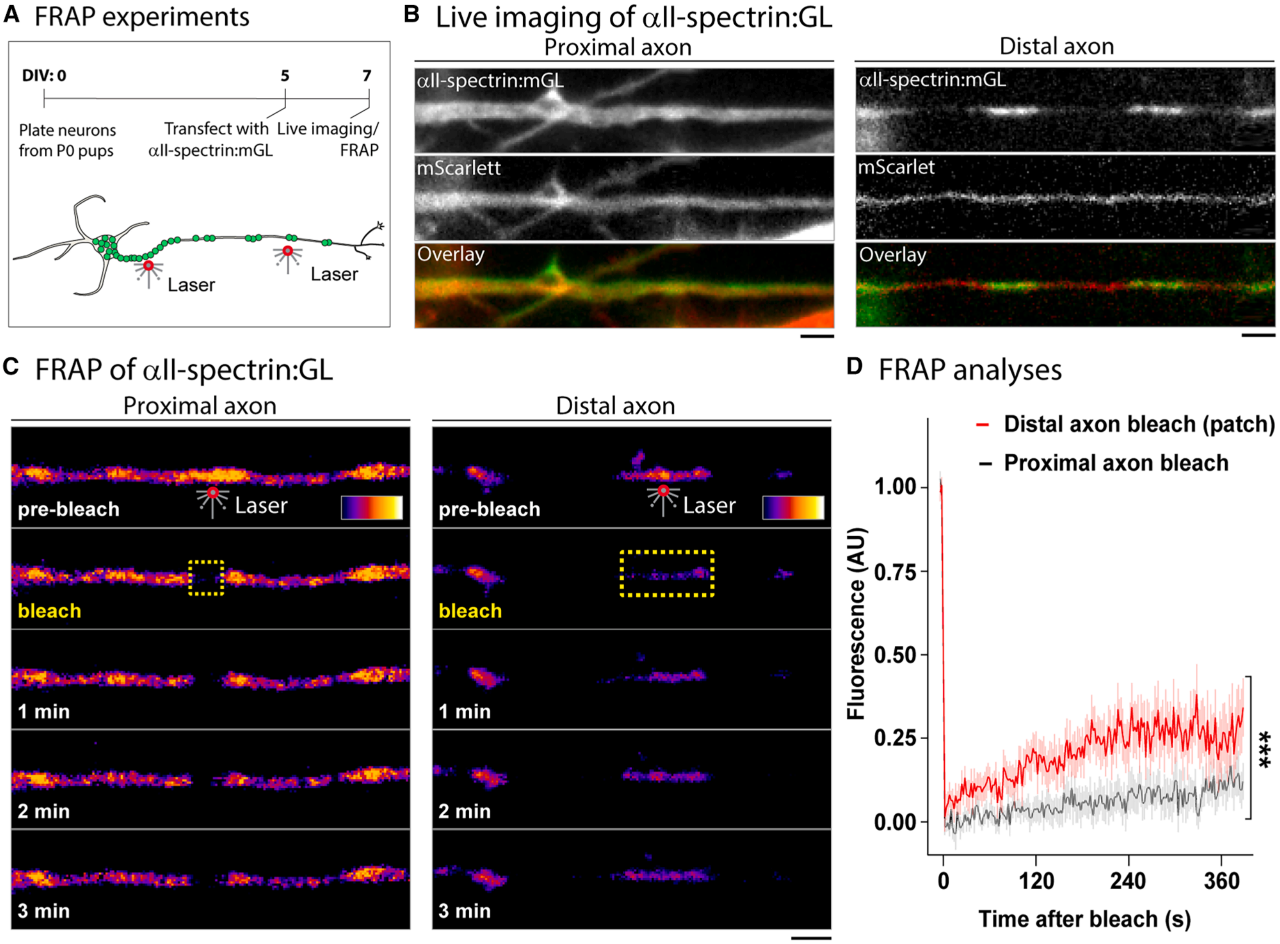

Figure 3. Spectrin in axonal patches can dynamically exchange with the axoplasm

(A) Schematic of live-cell imaging and FRAP experiments. 5 DIV neurons were co-transfected with αII-spectrin:mGL and mScarlet (volume filler). At 7 DIV, αII-spectrin:mGL was photobleached either in proximal axons (within 100 μm of soma), or in distal axonal patches.

(B) Live imaging of αII-spectrin:mGL in proximal and distal axons. Note distinct patches of fluorescence in distal axon, reminiscent of the endogenous spectrin pattern. These patches were largely stationary over ~15 min of imaging. Scale bars = 2 μm.

(C) Timelapse images show the recovery of αII-spectrin:mGL fluorescence following photobleaching (yellow dashed region) in the proximal axon or distal patches. Note that while the proximal axon shows minimal recovery of fluorescence – consistent with a stable lattice – distal axonal patches partially recover within minutes. Scale bars = 2 μm.

(D) Quantification of FRAP experiments shows significantly faster recovery in distal patches (n = 12/condition, in axons from 3 independent cultures, two-way ANOVA, interaction ***$p < 0.0001$).

multivalent interactions between SH3 domains are also known to participate in phase separation,[25,34,41] we generated a construct lacking this domain (ΔSH3). Additionally, we also generated constructs containing a variable number of spectrin repeats (encoding coiled-coil domains) but lacking EF-domains (15 or 9 repeats, see Figure 5A), because recent studies show that coiled-coil domains can also undergo phase separation. For instance, interactions between coiled-coil domains are known to drive the phase separation of several centrosomal proteins,[46,47] and many other proteins with coiled-coil domains are known to phase-separate, such as the structural Golgi protein GM130,[48] transcription factors and RNA-binding proteins,[49,50] endocytic proteins,[51] and others.[52–54] Even engineered proteins with coiled-coil domains can phase separate,[55] and simulations demonstrate that coiled-coil domains have a dramatically higher propensity for phase separation.[56]

Eliminating the SH3 domain (ΔSH3) did not abolish the ability of αII-spectrin to form inclusions in this assay (Figure 5B, left). However, interestingly, overexpression of *isolated* spectrin-repeat domains (SR5-20) – without the EF-hands or repeats 1–4 that allow tetramerization with βII-spectrin – formed inclusions in this experimental paradigm (Figure 5B, middle), whereas a construct containing only the first 9 spectrin repeats (SR1-9) was diffusely distributed (Figure 5B, right). Next, we tested putative condensate-like behaviors of these inclusions by FRAP and MOCHA-FRAP. Inclusions formed by both ΔSH3 and SR5-20 inclusions showed fluorescence recovery after full-bleaching, consistent with phase separation, though recovery of ΔSH3

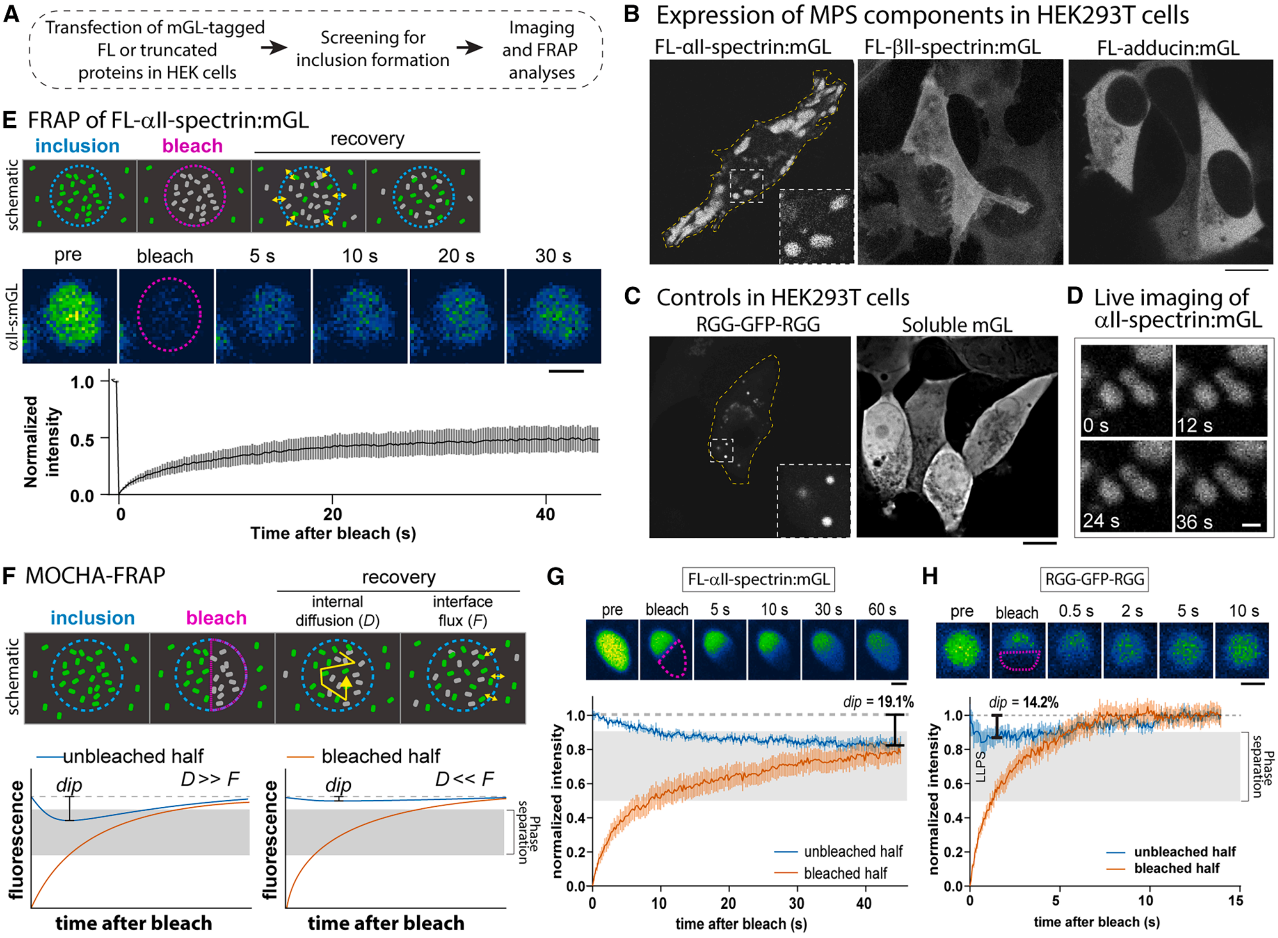

Figure 4. FL-αII-spectrin forms biomolecular condensates in heterologous cells

(A) Overall schematic of experiments expressing mGL-tagged FL or truncated αII/βII-spectrins/adducin in HEK293T cells.

(B) Expression of mGL-tagged FL αII-spectrin, βII-spectrin, and α-adducin in HEK293T cells. Note that FL-αII-spectrin formed distinct inclusions (zoomed in dashed inset), βII-spectrin showed a membranous localization (also see Video S2), and α-adducin was diffuse. Scale bars = 10 μm.

(C) Expression of a construct known to induce phase separation (engineered dimer of the RGG domain of yeast LAF1 protein fused to GFP), or soluble (untagged) mGL in HEK293T cells. Scale bars = 10 μm.

(D) Frames from timelapse imaging of αII-spectrin:mGL inclusions in HEK293T cells show that they are largely stationary and do not undergo merging or splitting. Scale bars = 1 μm.

(E) Top panel: Schematic showing kinetics of FRAP when a single inclusion is completely photobleached. Note that the recovery is due to the diffusion of fluorescent molecules from unbleached regions into the bleached region, across the surface of liquid droplets (small yellow arrows). Middle/bottom panels: FRAP of αII-spectrin droplets shows recovery of 40–50% of fluorescence within 45 s (*n* = 8, cells from 3 independent cultures, scale bars = 1 μm).

(F) Top: Schematic showing the principle of MOCHA-FRAP experiments, in which one-half of a fluorescent inclusion is photobleached. Note that FRAP in this scenario is due to the diffusion of fluorescent molecules from the unbleached region (long yellow arrow), as well as from across the surface of putative droplets (small yellow arrows). Later in discussion: Assuming that the fluorescence redistributes within the inclusion at diffusion rate *D* and fluorescence in the droplet as a whole recover at interface flux-rate *F*, theoretical graphs show fluorescence of both unbleached and bleached droplet halves in a scenario in which $D \gg F$ (left), or when $D \ll F$ (right). The depth of the fluorescence dip in the unbleached half correlates to the balance between these two rates and is an indicator of liquid-like behavior.

(G) MOCHA-FRAP analyses of αII-spectrin:mGL inclusions. Top panel: Representative FRAP images of a single αII-spectrin:mGL inclusion (top). The bleached region is marked with a dashed red line; note recovery of fluorescence in the bleached region. Bottom panel: Quantitative graphs of unbleached and bleached regions, obtained using the MOCHA-FRAP workflow. Black vertical bar indicates a dip depth of 19.1% at the location of minimum fluorescence of the unbleached half, which falls within the expected range for phase separation in the MOCHA-FRAP model (*n* = 8, cells from 3 independent cultures). Scale bars = 1 μm.

(H) MOCHA-FRAP experiments on RGG-GFP-RGG droplets display fast internal redistribution and fluorescence recovery, with a dip depth of 14.2%, which is consistent with phase separation (*n* = 9, cells from 3 independent cultures). Scale bars = 1 μm.

was more restricted, perhaps due to the EF-domains (Figure 5C). MOCHA-FRAP analyses of both ΔSH3 and SR5-20 showed that dip-depths for both deletion constructs were within the expected range for phase separation (Figure 5D). MOCHA-FRAP also allows for the calculation of internal diffusion, as the difference between total droplet fluorescence recovery and recovery of

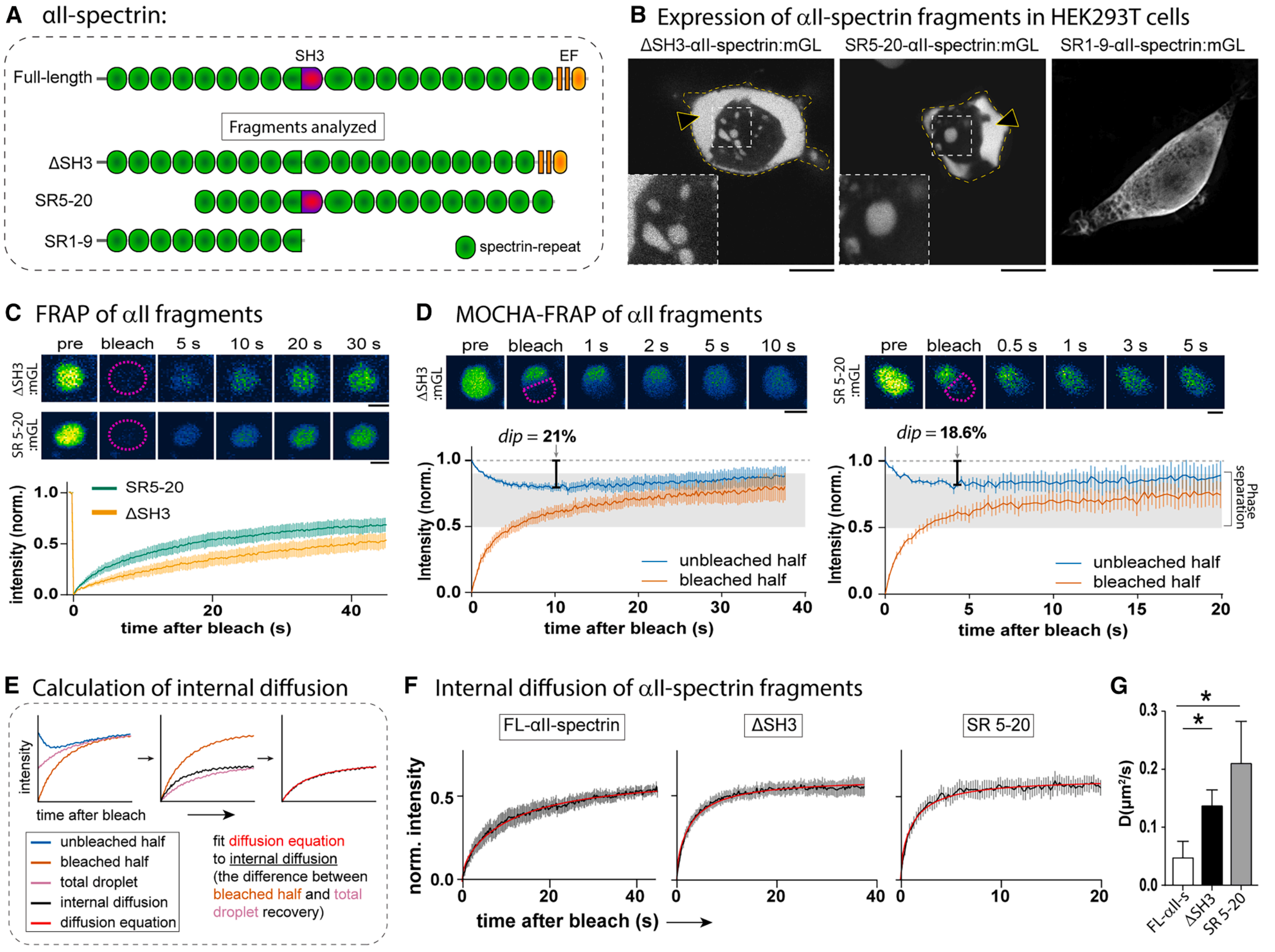

Figure 5. Spectrin-repeat domains within FL-αII-spectrin show droplet-like behavior

(A) Schematic showing FL and domain-deletion constructs of αII-spectrin that were tested for droplet formation in HEK293T cells. Constructs lacking the SH3 domain (ΔSH3), the N- and C-termini (SR5-20), or spectrin repeats 10–20 (SR1-9) were tagged with mGL.

(B) Discrete, rounded inclusions were seen with ΔSH3 and SR5-20, but not with SR1-9 (highlighted in zoomed inset). Large swaths of fluorescence are also seen (black arrowheads), which may be related to the extent of over-expression and biophysical properties (also see Figure S3 and results, scale bars = 10 μm).

(C) Full-inclusion FRAP analyses of mGL-tagged ΔSH3 and SR5-20 (top: images –bleached region outlined, bottom: FRAP-curves). Note that both αII-spectrin fragments show ~40–60% fluorescence recovery (data obtained in cells from three independent cultures, scale bars = 1 μm).

(D) MOCHA-FRAP analyses of mGL-tagged ΔSH3 and SR5-20 inclusions (top: images – dashed red line marks bleached region, bottom: fluorescence-curves from unbleached and bleached halves). Black bars indicate the dip depths at the locations of minimum fluorescence of the unbleached half. Note that in both cases, the dip-depth falls within the predicted range for phase separation, highlighted in gray (n = 7–10/condition, cells from 3 independent cultures, scale bars = 1 μm).

(E) Schematic depicting steps for determining internal diffusion coefficient *D* from MOCHA-FRAP experiments. *D* is calculated from the Brownian diffusion curves (red) fit to the internal diffusion (black), which is equal to the fluorescence recovery of the bleached half (orange) with the total droplet recovery (pink) subtracted.

(F) Graphs of internal diffusion from MOCHA-FRAP experiments with FL-αII-spectrin as well as SR5-20 and ΔSH3 constructs, with diffusion equation fits in red (n = 7–10, cells from 3 independent cultures).

(G) Quantification of *D* from individual diffusion curves from populations of droplets, summarized in (F). Deletion of the N/C-termini or SH3-domain results in faster internal diffusion than within full-length protein droplets (mean ± SEM, one-way ANOVA with Dunn post hoc *, $p < 0.05$).

the bleached half represents only the movement of fluorescence within the droplet (Figure 5E). We fit a standard Brownian diffusion equation (see STAR Methods) to this difference and found that though the deletion of the N- and C-termini or the SH3 domain did not fully ablate droplet formation, these deletions increased the internal diffusion rate of both ΔSH3 and SR5-20 constructs (Figures 5F and 5G). Collectively, the data indicate that isolated spectrin-repeats can trigger condensate formation.

Eliminating actin and membrane-binding domains of βII-spectrin facilitates condensate-formation

As FL-βII-spectrin did not readily exhibit phase separation when expressed in HEK293T cells, we next examined domain deletions of βII-spectrin. FL-βII-spectrin has calponin-homology actin-binding domains (CH-CH) at its N-terminus, followed by 17 spectrin repeats – consisting of coiled-coil domains – and a plasma-membrane binding pleckstrin homology (PH) domain

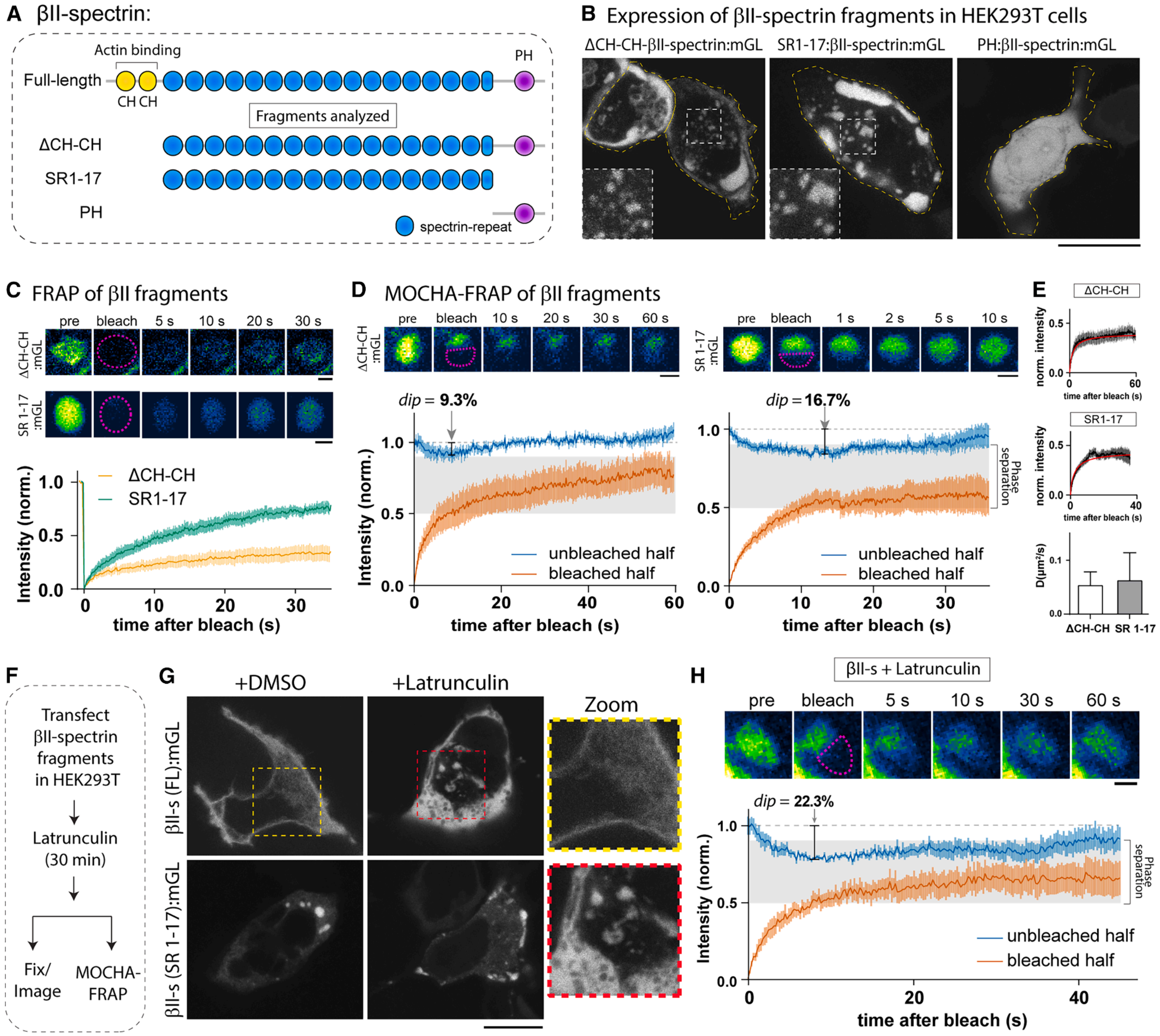

Figure 6. Isolated spectrin-repeats in βII-spectrin can form condensates

(A) Schematic showing full-length (FL) and domain-deletion constructs of βII-spectrin that were tested for droplet formation in HEK293T cells. Constructs lacking the actin-binding calponin homology domains (ΔCH-CH), containing only the 17 spectrin repeats (SR1-17), or containing only the C-terminal membrane-binding pleckstrin homology domain (PH) were tagged with mGL.

(B) Discrete inclusions were seen with ΔCH-CH and SR1-17, but not with PH (highlighted in zoomed inset), suggesting that eliminating actin- and membrane-binding promoted inclusion-formation (scale bars = 10 μm).

(C) Full-inclusion FRAP analyses of mGL-tagged ΔCH-CH and SR1-17 (top: images – dashed red line marks bleached region, bottom: FRAP-curves). Note that recovery was faster when both actin- and membrane-binding domains were deleted (SR1-17, compared to DCH-CH; n = 7–9/condition, in cells from 3 independent cultures; scale bars = 1 μm).

(D) MOCHA-FRAP analyses of mGL-tagged ΔCH-CH and SR1-17 inclusions (top: images – dashed red line marks bleached region, bottom: fluorescence-curves from unbleached and bleached halves). Black bars indicate the dip depths at the locations of minimum fluorescence of the unbleached half. Note that only the dip-depth of SR1-17 falls within the predicted range for phase separation, highlighted in gray (n = 7–9/condition, cells from 3 independent cultures, scale bars = 1 μm).

(E) Internal diffusion graphs with fitted curves in red, and graphs of *D* calculated from population analyses (see method in Figures 5E–5G). Internal diffusion rates for ΔCH-CH and SR1-17 are similar, suggesting that MOCHA-FRAP differences may be driven by interface flux. Mean ± SEM, data from 7 to 9 droplets/cells from 3 independent cultures. Scale bars = 1 μm.

(F) Testing the role of actin filaments in βII-spectrin droplet-formation. HEK293T cells transfected with FL-βII-spectrin or SR1-17-βII-spectrin were treated with 20 μM latrunculin A for 30 min to disrupt F-actin (or 4% DMSO as controls).

(legend continued on next page)

at its C-terminus (Figure 6A). Analyses of disorder-probability also suggested short putative disordered segments flanking the PH domain (Figure S7E), prompting us to examine this segment as well. Unlike FL-βII-spectrin, which was enriched near the cell surface, striking inclusions were seen with overexpression of βII-spectrin fragments lacking the actin-binding (ΔCH-CH) domain, or a construct containing only spectrin-repeats (SR 1–17); while a fragment containing the PH-domain and predicted disordered regions was cytosolic (Figure 6B). FRAP of SR1-17 inclusions showed substantial recovery after photobleaching – suggesting droplet-like behavior – but recovery for ΔCH-CH inclusions was much lower (Figure 6C). MOCHA-FRAP analyses supported this observation, showing that only the dip-depth of SR 1–17 inclusions fell within the range of droplet-like behavior (Figure 6D). Despite these differences in dip-depths, we did not find significant differences between internal diffusion rates of SR1-17 and ΔCH-CH inclusions (Figure 6E). We also overexpressed fragments of adducin in HEK293T cells, but they either generated aggregates that did not behave like biomolecular condensates in FRAP assays, or were soluble like the FL protein (Figure S8). Though the biological significance of these results is unclear, one possibility is that adducin molecules are passively recruited to spectrin condensates. In support of this, though FL-adducin was soluble in HEK293T cells when transfected alone (see Figure 4B, right), it colocalized with αII-spectrin inclusions when co-transfected with FL-αII-spectrin (Figures S9A–S9C). Co-transfection of α/β-spectrins and adducin in HEK cells showed that the majority of inclusions contained all three proteins (Figures S9D and S9E).

Taken together, quantitative analyses of βII-spectrin (FL and fragments) indicate that removing both the actin- and membrane-binding domains facilitates the formation of biomolecular condensates. Specifically, the isolated spectrin repeats of βII-spectrin showed the most robust evidence for phase separation. One prediction of this model is that preventing the association of FL-βII-spectrin with F-action should also trigger condensate-formation. To test this, we transfected HEK293T cells with FL-βII-spectrin (or SR1-17 as a control), treated the cells with latrunculin to disrupt actin filaments, and examined the cells by imaging and MOCHA-FRAP (Figure 6F). Interestingly, while FL-βII-spectrin was membranous in control cells as expected, treatment with latrunculin induced the formation of condensate-like structures in cells (Figure 6G, top panels). Latrunculin treatment had little effect on pre-existing SR1-17 condensates, though there was a change in morphology, perhaps due to an increase in liquid-like behavior (Figure 6G, bottom panels). MOCHA-FRAP of latrunculin-induced FL-βII-spectrin inclusions showed that the fluorescence dip-depth was within the range for phase separation (Figure 6H).

Following up on the logic that actin incorporation can facilitate the formation of a mature MPS, a prediction of our model is that an excess of actin in distal axons would augment actin incorporation into spectrin and decrease its patchy distribution (or enhance continuity of spectrin staining). To test this, we transfected neurons with GFP:actin – or soluble untagged GFP as controls – and examined the distribution of endogenous spectrin in axons of actin-overexpressing neurons, compared to controls (Figure 7A). Indeed, exogenous overexpression of actin augments the continuity of endogenous αII-spectrin in distal axons (Figures 7B and 7C). Further experiments suggest that the augmented distal-continuity is due to increased co-assembly of actin and spectrin (Figures 7D–7F), further supporting a model where the incorporation of actin facilitates the transition from condensates to a mature axonal MPS.

Early overexpression of condensate forming spectrin-repeats disrupt endogenous MPS assembly

Previous studies have shown that cytoskeleton-disrupting drugs can disassemble the MPS, but intrinsic structural determinants of MPS assembly are less clear. Our experiments advocate a model where α/β-spectrin repeats can organize into biomolecular condensates that form a nidus from which the axonal MPS is ultimately assembled. If so, we reasoned that the overexpression of condensate-forming spectrin-repeat fragments in neurons – before the axonal MPS is fully assembled – would interfere with putative endogenous phase separation mediated by spectrins, leading to a disruption of the MPS. However, following this logic, overexpression of the same fragments after the establishment of the axonal MPS would have little effect in the short-term, due to the known stability of the mature lattice structure.[19] To test this idea, we overexpressed condensate-forming βII-spectrin-repeat fragment (SR1-17, tagged with mScarlet) in cultured hippocampal neurons, either during MPS assembly (3 DIV), or after the proximal-MPS is expected to be established (7 DIV), and examined periodicity within 100 μm from the soma using structured illumination microscopy (Figure 8A). Like HEK cells, SR1-17 overexpression led to large inclusions in the neuronal soma that scaled with expression (Figures 8B, S10A). These SR1-17 inclusions sequestered endogenous MPS components, though adducin was conspicuously excluded (Figures 8C, S10B, and S10C). Note that the βII-spectrin antibody used in these experiments recognizes an epitope at the C-terminus of the protein and is not expected to see the over-expressed SR1-17 fragment. Neuronal SR1-17 inclusions also show recovery in FRAP experiments (Figure 8D), suggesting condensate-like behavior, and we posit that such large inclusions would likely interfere with innate physiologic processes of MPS assembly.

Next, we examined the effects of SR1-17 overexpression on the organization of proximal MPS by Structured Illumination Microscopy (SIM), which allowed us to resolve the periodic

---

(G) Top panels show that upon latrunculin treatment, there is a redistribution of FL-βII-spectrin from its normal membranous distribution to intracellular inclusions (zoomed insets on the right). Bottom panels show the effects of latrunculin on SR1-17 inclusions. Representative images shown, scale bars = 10 μm.

(H) MOCHA-FRAP analyses of FL-βII-spectrin inclusions formed after latrunculin-treatment. Top panel shows time-lapse images of an inclusion that was partially photobleached (bleached region highlighted by a red dashed line), bottom panel shows curves from MOCHA-FRAP analyses. Note that the dip-depth (22.3%, black vertical bar) is within the expected range for phase separation (gray box; $n = 6$ from 3 independent cultures; scale bars = 1 μm).

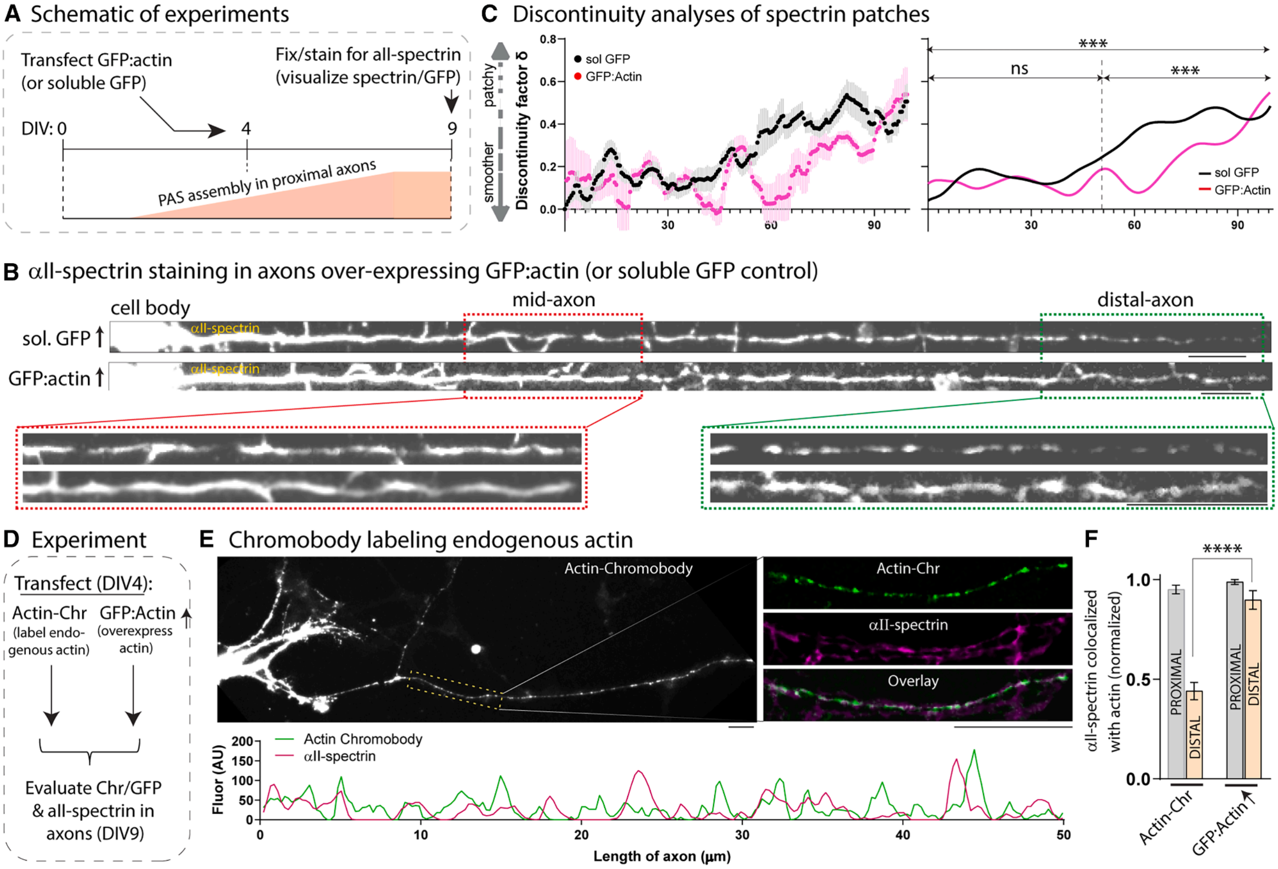

Figure 7. Actin overexpression attenuates spectrin discontinuity in distal axons

(A) Schematic showing the design of experiments to overexpress actin and evaluate endogenous spectrin.

(B and C) Examples of αII-spectrin staining in axons transfected with GFP:actin (or soluble GFP as controls). Note actin overexpression led to decreased spectrin patchiness (increased continuity) in distal axons, quantified in (C) using the "discontinuity analyses" algorithm (at least 5–6 neurons/condition, three separate cultures, ***$p < 0.0001$).

(D–F) Neurons were either transfected with actin-Chromobody (to label endogenous actin), or with GFP:actin (to overexpress actin), and incorporation of endogenous or overexpressed actin into spectrin-patches was evaluated. Note that while endogenously labeled actin showed scant colocalization with spectrin patches as expected (E), actin-overexpression led to more actin/spectrin colocalization (F), suggesting greater incorporation of actin into spectrin patches in the latter scenario (mean ± SEM, unpaired *t* test with Welch's correction, ****$p < 0.0001$). Scale bars in (E) = 20 μm.

structure of the MPS and obtain a large number of multicolor images of transfected axons, necessary for quantification. As shown in Figures 8E and 8F, expression of mScarlet-tagged SR1-17 at 3 DIV disrupted the MPS in proximal axons, whereas the expression of soluble mScarlet had no effect. On the other hand, when SR1-17:mScarlet was overexpressed at 7 DIV – a time when the MPS is expected to be established in the proximal axon – there was only a small (non-significant) effect on the periodic structure (Figures S10D and S10E). Although the SR1-17 accumulations are somewhat artificial, these experiments show that: 1) Spectrin-repeats alone *can* form condensate-like structures in neurons; and 2) Interfering with the physiologic process of condensate-formation during the period of MPS-assembly (but not after it is established) can disrupt the MPS. Taken together, these observations support a model where isolated coiled-coil domains can trigger condensates, and further underscore the importance of phase separation in the eventual organization of the MPS.

DISCUSSION

We started these experiments to find a plausible explanation on how the MPS attains its intricate, fully assembled periodic lattice in axons. In line with previous studies,[6,21] we found that as neurons grow, the MPS first assembles in the most proximal part of the axon, and the timing of this assembly coincides with the formation of the AIS. However, as axons develop, we also saw focal patches in distal axons that contained spectrins and adducin, but little F-actin (note that these distal axonal patches are distinct from the transient nanometer-sized defects in the proximal MPS described recently[57]). Our super-resolution microscopy showed that these distal patches do not have an organized lattice, and although they appear stable by live imaging, FRAP experiments showed that molecules within these patches can exchange with the surrounding axonal cytoplasm – a behavior consistent with phase separation. Expression of FL MPS-constituent proteins and domain-fragments in

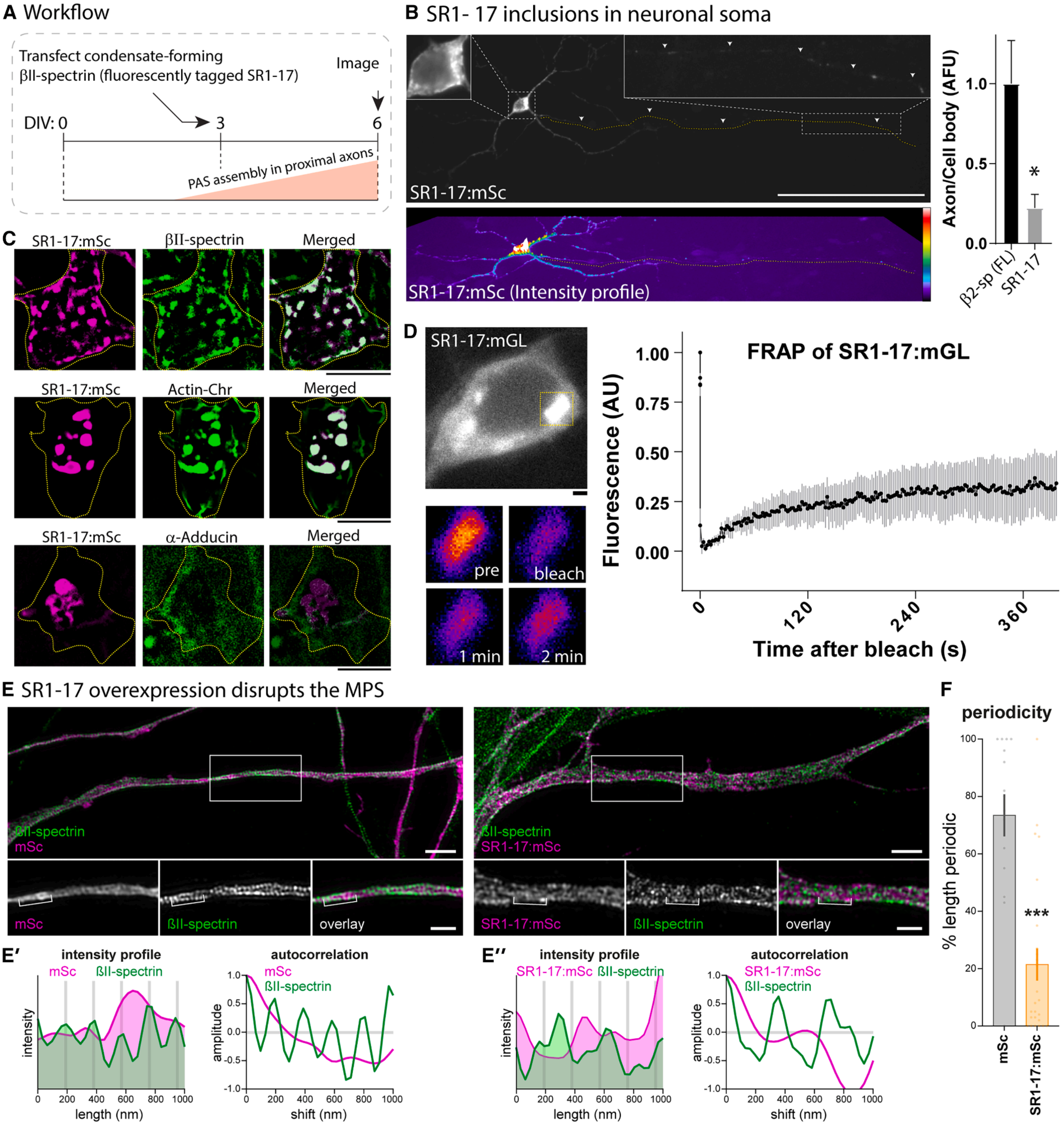

Figure 8. Early overexpression of minimal spectrin repeats disrupts endogenous MPS assembly in neurons

(A) Overall experimental design: Spectrin repeats of βII-spectrin (SR1-17:mScarlet) or soluble mScarlet were transfected in cultured hippocampal neurons either during (3–6 DIV), or after (7–10 DIV) the establishment of the endogenous MPS in the proximal axon (region within 100 μm from soma). Neurons were subsequently fixed, stained with an antibody against the C-terminus of βII-spectrin (that would label endogenous βII-spectrin but not the transfected SR1-17), and spectrin periodicity in axons was evaluated by SIM.

(B) SR1-17:mScarlet formed large inclusions in the neuronal soma with scant fluorescence in axons (marked by line/arrowheads, transfected DIV 7, analyzed DIV 10). Relative intensities of FL-βII-spectrin:mScarlet and SR1-17:mScarlet overexpression is quantified on the right (6–7 transfected neurons were analyzed for each condition from 2 separate coverslips. *, $p < 0.05$, also see Figure S10A).

(C and D) Neuronal SR1-17 inclusions also contained βII-spectrin (endogenous, see results for explanation) and actin, but no adducin (also see Figure S10B). Neurons were transfected at 3 DIV with SR 1–17:mScarlet and Actin-Chromobody, and fixed at 6 DIV (representative data from ∼15 neurons for each condition, 3 coverslips). FRAP recovery of neuronal SR1-17:mGL inclusions shown in (D).

(legend continued on next page)

heterologous cells collectively indicates that spectrin fragments from both α/β-spectrins can form biomolecular condensates. These experiments also showed that preventing the association of βII-spectrin with actin filaments and membranes triggered the formation of condensates, suggesting that the presence or absence of F-actin in the axon could regulate condensate-like behavior of the MPS components and help assemble the periodic lattice. Finally, overexpressing condensate-triggering spectrin repeats early in neuronal development – during the establishment of the MPS – disrupted its periodicity in the proximal axon, suggesting a role for phase separation in MPS assembly.

A condensation-assembly model for building the periodic axonal cytoskeleton

Previous studies have proposed a propagation model where the lattice initially assembles next to the cell-body/axon junction, and then propagates distally along the length of the axon.[21] Another study observed βII-spectrin patches in distal growing axons but did not evaluate these structures further; proposing a model where the MPS originates at the axon-tip, with distal patches coalescing over time to form a continuous organized lattice.[22] However, there is no direct evidence to support these contrasting models. Continuous, templated assembly of the MPS toward the distal axon – as predicted by the propagation model – or coalescence of the distal spectrin patches into an assembled periodic lattice has not been observed. Our experiments advocate a new model where biomolecular condensation and actin filaments play roles in the biogenesis and assembly of the axonal MPS, respectively.

In line with previous observations,[6,21,22] we found that as axons begin to grow, the MPS is first assembled in the most proximal regions. Though the mechanistic events underlying this initial assembly are unclear, it may relate to the proximity of the initial segment to the soma, where components of the MPS are synthesized. A related possibility is that the high concentration of spectrin and actin in proximal regions favor rapid transition of patches into MPS. At a time when the MPS is assembled near the soma-axon junction, distal axons have discrete patches containing spectrins and adducin, and we propose that the patches act as local depots for supplying the building blocks necessary to assemble the MPS. What are the mechanisms underlying the assembly of these axonal patches? Taken together, our experiments in neurons and non-neuronal cells suggest that the spectrin repeats within α/β-spectrins form biomolecular condensates that provide the necessary environment for concentrating components of the MPS into distal axonal patches. While many biomolecular condensates are dynamic and show dripping and fusing behavior,[41,55,58,59] axonal patches are largely static and do not coalesce over a timescale of minutes (Video S1), but exchange molecules with the surrounding cytoplasm (Figures 3C and 3D) – consistent with known behaviors of solid-like condensates.[34,60,61] The solid-like behavior of spectrin inclusions – both in neurons and HEK293T cells (see Figures 4, 5, and 6) – was unexpected, but may reflect a need to place MPS building-blocks at precise positions along the growing axon. Notably, solid phases are recognized in many native organelles that are thought to assemble by phase separation.[41,62,63]

How are components from the axonal patches eventually integrated into a mature periodic lattice? Though we do not have complete answers to this difficult question, three observations suggest that actin filaments may play a role. First, spectrin/adducin patches tend to form in axonal regions that have relatively less F-actin (Figure 2), suggesting that the paucity of actin filaments may be a driving force for condensation in this setting. Second, while βII-spectrin:mGL largely localizes to the plasma membrane in HEK293T cells, deleting actin- and membrane-binding domains of βII-spectrin triggered phase separation (Figure 6). Third, overexpression of actin increased the continuity of spectrin in distal axons (Figure 7), suggesting that actin incorporation augmented the formation of a mature MPS. Intriguingly, recent studies suggest that *any* condensate-forming protein that physiologically binds to actin can bundle actin filaments by recruiting actin monomers via flexible, multivalent interactions between actin-binding domains within the condensate-protein and cytosolic actin.[64,65] Extrapolating this concept to our studies, one possibility is that actin-binding domains in βII-spectrin molecules within axonal condensates could recruit cytosolic actin from the axon shaft, providing an environment where spectrin and actin can assemble into a lattice structure. Such assembly might be related to the known rearrangement of actin into ring-shaped bundles when confined to micron-sized spherical droplets *in vitro*.[66] Future studies using biophysical modeling, artificial reconstitution of the lattice, or *in vitro* phase separation assays with recombinant proteins may give a more detailed view of these events.

Taken together, these observations are consistent with a scenario where gradual accumulation of actin filaments in the distal axon would translocate spectrins and adducin – components of the MPS that bind to each other – from the axonal patches to the subplasmalemmal network of actin filaments, where they can be assembled into the periodic lattice (Figure 9). We also posit that overall, the proximal to distal assembly of the MPS would be facilitated by the larger size/increased density of spectrin patches in regions closer to the AIS/proximal-axon (Figure 1F), likely generated by the anterogradely biased axonal transport of MPS components from the soma into the axon (Figure 9). It is also interesting to consider that the lack of a rigid lattice in the distal axons may be an

---

(E) Periodicity in proximal axons of neurons transfected with mScarlet-tagged SR1-17 (or soluble mScarlet) at 3 DIV. Note that the overexpression of SR1-17 impeded the assembly of the MPS; zoomed insets later in discussion.

(E) Fluorescence intensity profiles and autocorrelation analysis of axonal segments from (E) using SIM – zoomed insets, analyzed region marked by white brackets. Note disrupted periodicity upon transfection with SR1-17.

(F) Quantification of the βII-spectrin periodicity in proximal axons. Periodicity in neurons expressing SR1-17:mSc was significantly lower than in neurons expressing soluble mScarlet (mean ± SEM, unpaired *t* test, nonparametric, Kolmogorov-Smirnoff, data from 15 to 25 neurons from 3 independent cultures. ***, $p < 0.0001$). Scale bars: (B) = 100 μm; (C) = 10 μm; (D) 2 μm; (E) Top panels = 2 μm, bottom panels = 1 μm.

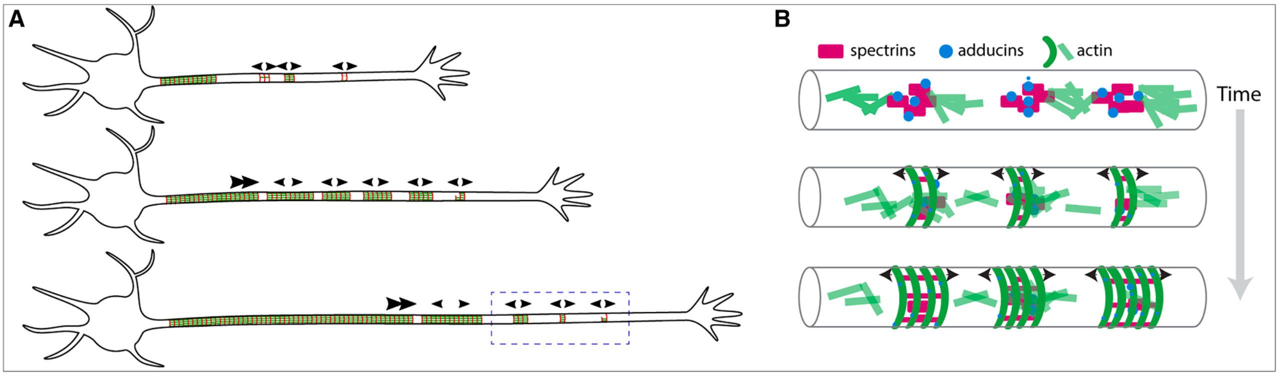

Figure 9. Model for MPS assembly during development

(A) The MPS is first established in the most proximal part of the axon near cell bodies, followed by patches of spectrin/adducin (condensates) in more distal regions. Over time, the incorporation of actin into the patches generates a periodic lattice that extends laterally from the patches. A greater size/density of patches in axonal segments closer to the soma – presumably due to biased deposition of components via axonal transport – leads to a proximal to the distal extension of the MPS as the axon extends.

(B) A zoomed-in view of proposed mechanistic events.

evolutionary adaptation to allow plasticity of the distal axon and growth cone. Along these lines, our data also suggest that spectrin patches are present in mature axons as well, particularly in axon segments that are away from synapses (Figure S2). A related scenario is that preformed spectrin patches may slide and ‘‘interlock’’ to form a continuous MPS in a Lego-like fashion. Though we did not see any movement of the patches over time, our imaging only extended to 15 min, so we cannot exclude this possibility.

Spectrin repeats as mediators of biomolecular condensation

Recent conceptual advances support our model. Formation of the centrosome and central spindle relies on the biomolecular condensation of coiled-coil proteins,[47] and many of the component proteins, such as pericentrin, spd-5, centrosomin, and MAP65/PRC1, can undergo phase separation.[34,67–69] Several other proteins known to undergo phase separation have coiled-coil domains,[48–54] and even proteins engineered to contain coiled-coil domains can be coaxed to form condensates.[42] Simulations show that as few as two coiled-coil domains can phase separate, and that the propensity to condensate scales up with the number of coiled-coil domains.[56,70] We found that isolated spectrin-repeat domains of α/β-spectrins can undergo phase separation in HEK293T cells (Figures 5 and 6). Spectrin repeats fold as coiled-coil helices, and this repeating structure is a defining feature of the spectrin superfamily that helps different isoforms of spectrin bind to each other.[45] Our data show that at high protein concentrations – such as conditions in the HEK293T cells after overexpression – coiled-coil domains of the same spectrin isoform can presumably self-associate into biomolecular condensates. Though it is unclear how such high concentrations of spectrins are achieved inside the axon, one possibility is that this is a combined effect of: a) the potential for FL-αII-spectrin to form condensates, and b) a paucity of actin filaments in distal axons that increases the propensity of FL-βII-spectrin to undergo phase separation (due to spectrin-repeats within its sequence). Since α/β-spectrins are typically present together as heterotetramers, presumably this would create foci with a high concentration of spectrin molecules. Regardless, our experiments add spectrins to the growing list of coiled-coil domain proteins that can undergo phase separation, and advocate a role for this process in the early assembly of higher-order cytoskeletal structures.

Limitations of the study

Our FRAP experiments in neurons rely on overexpression, which can change the localization of proteins. Though we have chosen low expressers for our experiments and spectrin patches are clearly seen in this setting, suggesting that the localization of proteins is not dramatically altered, the overexpression paradigm is a general concern. Similar caveats may apply to the setting where SR1-17 fragments are transfected in neurons, though the purpose here was to trigger condensate-formation by overexpression. Finally, though our collective data supports a scenario involving phase separation, we cannot exclude the possibility that the axonal patches represent some aggregated (non-condensate) form of spectrin tetramers.

RESOURCE AVAILABILITY

Lead contact

Further information and requests for resources and reagents should be directed to and will be fulfilled by the Lead Contact, Subhojit Roy (sroy@ucsd.edu).

Materials availability

All DNA-constructs generated for this study are available from the lead contact and may require material transfer agreements (MTAs).

Data and code availability

- Data: All data generated or analyzed during this study (raw and processed) are available from the lead contact upon request.
- Code: No new code was generated for this study.
- Other items: Any additional information required to reanalyze the data reported in this article is available from the lead contact upon request.

ACKNOWLEDGMENTS

This work was mostly supported by an NIH grant to S.R. (R01NS075233). Some imaging experiments were supported by a NINDS P30NS047101 grant to the UCSD microscopy core. C.L. acknowledges funding from the Agence National de la Recherche (ANR-20-CE13-0024, ANR-20-CE16-0021, ANR-21-CE42-0015), the Fédération pour la Recherche sur le Cerveau (AOE 16 "Espoir en tête" 2021) and thanks the INP NCIS imaging facility and Nikon Center of Excellence for Neuro-NanoImaging for service and expertise, with funding from Excellence Initiative of Aix-Marseille University, A*MIDEX, a French "Investissements d'Avenir" program through the Marseille Imaging (AMX-19-IET-002) and NeuroMarseille (AMX-19-IET-004) Institutes.

AUTHOR CONTRIBUTIONS

NB and SR originally conceived these studies; CL and RS made substantial conceptual contributions. NB and RS performed most of the experiments in SR's laboratory, while super-resolution experiments were performed in CL's laboratory: AD, FP, and TW performed the SIM experiments and their analysis, CL and CP performed the STORM experiments, and CL performed live-cell imaging experiments using constructs prepared by NJ. NB and SR wrote and assembled the article with contributions from CL and RS. AB performed some cell biology experiments, LP and FS were involved in biochemistry and construct-production. PK performed imaging of mouse brains.

DECLARATION OF INTERESTS

The authors declare no competing interests.

DECLARATION OF GENERATIVE AI AND AI-ASSISTED TECHNOLOGIES IN THE WRITING PROCESS

No AI/AI-assisted tools were used in the writing process.

STAR★METHODS

Detailed methods are provided in the online version of this paper and include the following:

- KEY RESOURCES TABLE
- EXPERIMENTAL MODEL AND SUBJECT DETAILS
    - ○ Animals and cell-lines
- METHOD DETAILS
    - ○ Plasmids, antibodies, and reagents
    - ○ Neuronal cultures, transfections, and immunocytochemistry
    - ○ Tissue processing and immunofluorescence staining
    - ○ Discontinuity factor
    - ○ STORM super-resolution microscopy
    - ○ SIM super-resolution microscopy
    - ○ SIM image analysis
    - ○ Live-cell spinning-disk imaging
    - ○ Axonal FRAP
    - ○ Droplet FRAP
- QUANTIFICATION AND STATISTICAL ANALYSIS
    - ○ FRAP quantification and other analyses
    - ○ Protein disorder prediction
    - ○ Statistical analysis

SUPPLEMENTAL INFORMATION

Supplemental information can be found online at https://doi.org/10.1016/j.isci.2025.114454.

Received: September 18, 2025
Revised: October 28, 2025
Accepted: December 11, 2025
Published: December 16, 2025

REFERENCES

1. Xu, K., Zhong, G., and Zhuang, X. (2013). Actin, spectrin, and associated proteins form a periodic cytoskeletal structure in axons. Science *339*, 452–456. https://doi.org/10.1126/science.1232251.
2. Vassilopoulos, S., Gibaud, S., Jimenez, A., Caillol, G., and Leterrier, C. (2019). Ultrastructure of the axonal periodic scaffold reveals a braid-like organization of actin rings. Nat. Commun. *10*, 5803–5813. https://doi.org/10.1038/s41467-019-13835-6.
3. Unsain, N., Stefani, F.D., and Cáceres, A. (2018). The actin/spectrin membrane-associated periodic skeleton in neurons. Front. Synaptic Neurosci. *10*, 1–8. https://doi.org/10.3389/fnsyn.2018.00010.
4. Leterrier, C. (2021). Putting the axonal periodic scaffold in order. Curr. Opin. Neurobiol. *69*, 33–40. https://doi.org/10.1016/j.conb.2020.12.015.
5. He, J., Zhou, R., Wu, Z., Carrasco, M.A., Kurshan, P.T., Farley, J.E., Simon, D.J., Wang, G., Han, B., Hao, J., et al. (2016). Prevalent presence of periodic actin-spectrin-based membrane skeleton in a broad range of neuronal cell types and animal species. Proc. Natl. Acad. Sci. USA *113*, 6029–6034. https://doi.org/10.1073/pnas.1605707113.
6. D'Este, E., Kamin, D., Göttfert, F., El-Hady, A., and Hell, S.W. (2015). STED Nanoscopy Reveals the Ubiquity of Subcortical Cytoskeleton Periodicity in Living Neurons. Cell Rep. *10*, 1246–1251. https://doi.org/10.1016/j.celrep.2015.02.007.
7. D'Este, E., Kamin, D., Velte, C., Göttfert, F., Simons, M., and Hell, S.W. (2016). Subcortical cytoskeleton periodicity throughout the nervous system. Sci. Rep. *6*, 22741–22748. https://doi.org/10.1038/srep22741.
8. Hammarlund, M., Jorgensen, E.M., and Bastiani, M.J. (2007). Axons break in animals lacking β-spectrin. J. Cell Biol. *176*, 269–275. https://doi.org/10.1083/jcb.200611117.
9. Krieg, M., Stühmer, J., Cueva, J.G., Fetter, R., Spilker, K., Cremers, D., Shen, K., Dunn, A.R., and Goodman, M.B. (2017). Genetic defects in β-spectrin and tau sensitize C. Elegans axons to movement-induced damage via torque-tension coupling. eLife *6*, e20172. https://doi.org/10.7554/eLife.20172.
10. Dubey, S., Bhembre, N., Bodas, S., Veer, S., Ghose, A., Callan-Jones, A., and Pullarkat, P. (2020). The axonal actin-spectrin lattice acts as a tension buffering shock absorber. eLife *9*, e51772. https://doi.org/10.7554/eLife.51772.
11. Zhou, R., Han, B., Xia, C., and Zhuang, X. (2019). Membrane-associated periodic skeleton is a signaling platform for RTK transactivation in neurons. Science *365*, 929–934. https://doi.org/10.1126/science.aaw5937.
12. Li, H., Yang, J., Tian, C., Diao, M., Wang, Q., Zhao, S., Li, S., Tan, F., Hua, T., Qin, Y., et al. (2020). Organized cannabinoid receptor distribution in neurons revealed by super-resolution fluorescence imaging. Nat. Commun. *11*, 5699. https://doi.org/10.1038/s41467-020-19510-5.
13. Costa, A.R., Sousa, S.C., Pinto-Costa, R., Mateus, J.C., Lopes, C.D., Costa, A.C., Rosa, D., Machado, D., Pajuelo, L., Wang, X., et al. (2020). The membrane periodic skeleton is an actomyosin network that regulates axonal diameter and conduction. eLife *9*, e55471. https://doi.org/10.7554/eLife.55471.
14. Wang, T., Li, W., Martin, S., Papadopulos, A., Joensuu, M., Liu, C., Jiang, A., Shamsollahi, G., Amor, R., Lanoue, V., et al. (2020). Radial contractility of actomyosin rings facilitates axonal trafficking and structural stability. J. Cell Biol. *219*, e201902001. https://doi.org/10.1083/jcb.201902001.
15. Lorenz, T., and Willard, M. (1978). Subcellular fractionation of intra-axonally transported polypeptides in the rabbit visual system. Proc. Natl. Acad. Sci. USA *75*, 505–509. https://doi.org/10.1073/pnas.75.1.505.
16. Cheney, R., Hirokawa, N., Levine, J., and Willard, M. (1983). Intracellular movement of fodrin. Cell Motil. *3*, 649–655. https://doi.org/10.1002/cm.970030529.
17. Willard, M., Baitinger, C., and Cheney, R. (1987). Translocations of fodrin and its binding proteins. Brain Res. Bull. *18*, 817–824. https://doi.org/10.1016/0361-9230(87)90221-8.

18. Roy, S. (2020). Finding order in slow axonal transport. Curr. Opin. Neurobiol. *63*, 87–94. https://doi.org/10.1016/j.conb.2020.03.015.
19. Chakrabarty, N., Dubey, P., Tang, Y., Ganguly, A., Ladt, K., Leterrier, C., Jung, P., and Roy, S. (2019). Processive flow by biased polymerization mediates the slow axonal transport of actin. J. Cell Biol. *218*, 112–124. https://doi.org/10.1083/jcb.201711022.
20. Glomb, O., Swaim, G., Munoz LLancao, P., Lovejoy, C., Sutradhar, S., Park, J., Wu, Y., Cason, S.E., Holzbaur, E.L.F., Hammarlund, M., et al. (2023). A kinesin-1 adaptor complex controls bimodal slow axonal transport of spectrin in Caenorhabditis elegans. Dev. Cell *58*, 1847–1863.e12. https://doi.org/10.1016/j.devcel.2023.08.031.
21. Zhong, G., He, J., Zhou, R., Lorenzo, D., Babcock, H.P., Bennett, V., and Zhuang, X. (2014). Developmental mechanism of the periodic membrane skeleton in axons. eLife *3*, e04581. https://doi.org/10.7554/eLife.04581.
22. Hofmann, M., Biller, L., Michel, U., Bähr, M., and Koch, J.C. (2022). Cytoskeletal assembly in axonal outgrowth and regeneration analyzed on the nanoscale. Sci. Rep. *12*, 14387. https://doi.org/10.1038/s41598-022-18562-5.
23. Gazal, N.G., Nahir, G.G., Maria, J.C.M., Guillermina, B., Anna, K.F.F., Sarah, L., Lale, G., Ghazal, H., Gilles, M., Agustín, A., et al. (2025). BetaII-Spectrin Gaps and Patches Emerge from the Patterned Assembly of the Actin/Spectrin Membrane Skeleton in Human Motor Neuron Axons. https://doi.org/10.1101/2025.05.09.653215.
24. Vorontsova, M.A., Chan, H.Y., Lubchenko, V., and Vekilov, P.G. (2015). Lack of Dependence of the Sizes of the Mesoscopic Protein Clusters on Electrostatics. Biophys. J. *109*, 1959–1968. https://doi.org/10.1016/j.bpj.2015.09.025.
25. Li, Y., Lubchenko, V., Vorontsova, M.A., Filobelo, L., and Vekilov, P.G. (2012). Ostwald-Like Ripening of the Anomalous Mesoscopic Clusters in Protein Solutions. J. Phys. Chem. B *116*, 10657–10664. https://doi.org/10.1021/jp303316s.
26. Chan, H.Y., and Lubchenko, V. (2019). A mechanism for reversible mesoscopic aggregation in liquid solutions. Nat. Commun. *10*, 2381. https://doi.org/10.1038/s41467-019-10270-5.
27. Yang, D.S., Saeedi, A., Davtyan, A., Fathi, M., Sherman, M.B., Safari, M.S., Klindziuk, A., Barton, M.C., Varadarajan, N., Kolomeisky, A.B., and Vekilov, P.G. (2021). Mesoscopic protein-rich clusters host the nucleation of mutant p53 amyloid fibrils. Proc. Natl. Acad. Sci. USA *118*, e2015618118. https://doi.org/10.1073/pnas.2015618118.
28. Sridharan, D., Brown, M., Lambert, W.C., McMahon, L.W., and Lambert, M.W. (2003). Nonerythroid αII spectrin is required for recruitment of FANCA and XPF to nuclear foci induced by DNA interstrand cross-links. J. Cell Sci. *116*, 823–835. https://doi.org/10.1242/jcs.00294.
29. Ray, S., Singh, N., Kumar, R., Patel, K., Pandey, S., Datta, D., Mahato, J., Panigrahi, R., Navalkar, A., Mehra, S., et al. (2020). α-Synuclein aggregation nucleates through liquid–liquid phase separation. Nat. Chem. *12*, 705–716. https://doi.org/10.1038/s41557-020-0465-9.
30. Zhang, F., Biswas, M., Massah, S., Lee, J., Lingadahalli, S., Wong, S., Wells, C., Foo, J., Khan, N., Morin, H., et al. (2023). Dynamic phase separation of the androgen receptor and its coactivators key to regulate gene expression. Nucleic Acids Res. *51*, 99–116. https://doi.org/10.1093/nar/gkac1158.
31. Schuster, B.S., Reed, E.H., Parthasarathy, R., Jahnke, C.N., Caldwell, R.M., Bermudez, J.G., Ramage, H., Good, M.C., and Hammer, D.A. (2018). Controllable protein phase separation and modular recruitment to form responsive membraneless organelles. Nat. Commun. *9*, 2985. https://doi.org/10.1038/s41467-018-05403-1.
32. Park, D., Wu, Y., Lee, S.E., Kim, G., Jeong, S., Milovanovic, D., De Camilli, P., and Chang, S. (2021). Cooperative function of synaptophysin and synapsin in the generation of synaptic vesicle-like clusters in non-neuronal cells. Nat. Commun. *12*, 263. https://doi.org/10.1038/s41467-020-20462-z.
33. Muzzopappa, F., Hummert, J., Anfossi, M., Tashev, S.A., Herten, D.P., and Erdel, F. (2022). Detecting and quantifying liquid–liquid phase separation in living cells by model-free calibrated half-bleaching. Nat. Commun. *13*, 7787. https://doi.org/10.1038/s41467-022-35430-y.
34. Woodruff, J.B., Ferreira Gomes, B., Widlund, P.O., Mahamid, J., Honigmann, A., and Hyman, A.A. (2017). The Centrosome Is a Selective Condensate that Nucleates Microtubules by Concentrating Tubulin. Cell *169*, 1066–1077.e10. https://doi.org/10.1016/j.cell.2017.05.028.
35. Emperador-Melero, J., Wong, M.Y., Wang, S.S.H., de Nola, G., Nyitrai, H., Kirchhausen, T., and Kaeser, P.S. (2021). PKC-phosphorylation of Liprin-α3 triggers phase separation and controls presynaptic active zone structure. Nat. Commun. *12*, 3057. https://doi.org/10.1038/s41467-021-23116-w.
36. Reber, S., Jutzi, D., Lindsay, H., Devoy, A., Mechtersheimer, J., Levone, B.R., Domanski, M., Bentmann, E., Dormann, D., Mühlemann, O., et al. (2021). The phase separation-dependent FUS interactome reveals nuclear and cytoplasmic function of liquid–liquid phase separation. Nucleic Acids Res. *49*, 7713–7731. https://doi.org/10.1093/nar/gkab582.
37. Parchure, A., Tian, M., Stalder, D., Boyer, C.K., Bearrows, S.C., Rohli, K.E., Zhang, J., Rivera-Molina, F., Ramazanov, B.R., Mahata, S.K., et al. (2022). Liquid–liquid phase separation facilitates the biogenesis of secretory storage granules. J. Cell Biol. *221*, e202206132. https://doi.org/10.1083/jcb.202206132.
38. Bennett, V., and Baines, A.J. (2001). Spectrin and ankyrin-based pathways: Metazoan inventions for integrating cells into tissues. Physiol. Rev. *81*, 1353–1392. https://doi.org/10.1152/physrev.2001.81.3.1353.
39. Bracha, D., Walls, M.T., Wei, M.T., Zhu, L., Kurian, M., Avalos, J.L., Toettcher, J.E., and Brangwynne, C.P. (2018). Mapping Local and Global Liquid Phase Behavior in Living Cells Using Photo-Oligomerizable Seeds. Cell *175*, 1467–1480.e13. https://doi.org/10.1016/j.cell.2018.10.048.
40. Sala, K., Corbetta, A., Minici, C., Tonoli, D., Murray, D.H., Cammarota, E., Ribolla, L., Ramella, M., Fesce, R., Mazza, D., et al. (2019). The ERC1 scaffold protein implicated in cell motility drives the assembly of a liquid phase. Sci. Rep. *9*, 13530. https://doi.org/10.1038/s41598-019-49630-y.
41. Banani, S.F., Lee, H.O., Hyman, A.A., and Rosen, M.K. (2017). Biomolecular condensates: organizers of cellular biochemistry. Nat. Rev. Mol. Cell Biol. *18*, 285–298. https://doi.org/10.1038/nrm.2017.7.
42. Bracha, D., Walls, M.T., and Brangwynne, C.P. (2019). Probing and engineering liquid-phase organelles. Nat. Biotechnol. *37*, 1435–1445. https://doi.org/10.1038/s41587-019-0341-6.
43. Brangwynne, C.P. (2013). Phase transitions and size scaling of membrane-less organelles. J. Cell Biol. *203*, 875–881. https://doi.org/10.1083/jcb.201308087.
44. Forman-Kay, J.D., Ditlev, J.A., Nosella, M.L., and Lee, H.O. (2022). What are the distinguishing features and size requirements of biomolecular condensates and their implications for RNA-containing condensates? RNA *28*, 36–47. https://doi.org/10.1261/rna.079026.121.
45. Djinovic-Carugo, K., Gautel, M., Ylänne, J., and Young, P. (2002). The spectrin repeat: a structural platform for cytoskeletal protein assemblies. FEBS Lett. *513*, 119–123. https://doi.org/10.1016/S0014-5793(01)03304-X.
46. Banani, S.F., Rice, A.M., Peeples, W.B., Lin, Y., Jain, S., Parker, R., and Rosen, M.K. (2016). Compositional Control of Phase-Separated Cellular Bodies. Cell *166*, 651–663. https://doi.org/10.1016/j.cell.2016.06.010.
47. Rios, M.U., Bagnucka, M.A., Ryder, B.D., Ferreira Gomes, B., Familiari, N.E., Yaguchi, K., Amato, M., Stachera, W.E., Joachimiak, Ł.A., and Woodruff, J.B. (2024). Multivalent coiled-coil interactions enable full-scale centrosome assembly and strength. J. Cell Biol. *223*, e202306142. https://doi.org/10.1083/jcb.202306142.
48. Rebane, A.A., Ziltener, P., LaMonica, L.C., Bauer, A.H., Zheng, H., López-Montero, I., Pincet, F., Rothman, J.E., and Ernst, A.M. (2020). Liquid–liquid phase separation of the Golgi matrix protein GM130. FEBS Lett. *594*, 1132–1144. https://doi.org/10.1002/1873-3468.13715.
49. Fang, X., Wang, L., Ishikawa, R., Li, Y., Fiedler, M., Liu, F., Calder, G., Rowan, B., Weigel, D., Li, P., and Dean, C. (2019). Arabidopsis FLL2

promotes liquid–liquid phase separation of polyadenylation complexes. Nature *569*, 265–269. https://doi.org/10.1038/s41586-019-1165-8.

50. Lu, Y., Wu, T., Gutman, O., Lu, H., Zhou, Q., Henis, Y.I., and Luo, K. (2020). Phase separation of TAZ compartmentalizes the transcription machinery to promote gene expression. Nat. Cell Biol. *22*, 453–464. https://doi.org/10.1038/s41556-020-0485-0.

51. Kozak, M., and Kaksonen, M. (2022). Condensation of Ede1 promotes the initiation of endocytosis. eLife *11*, e72865. https://doi.org/10.7554/eLife.72865.

52. Guseva, S., Milles, S., Jensen, M.R., Salvi, N., Kleman, J.P., Maurin, D., Ruigrok, R.W.H., and Blackledge, M. (2020). Measles virus nucleo- and phosphoproteins form liquid-like phase-separated compartments that promote nucleocapsid assembly. Sci. Adv. *6*, eaaz7095. https://doi.org/10.1126/sciadv.aaz7095.

53. Newton, J.C., Naik, M.T., Li, G.Y., Murphy, E.L., Fawzi, N.L., Sedivy, J.M., and Jogl, G. (2021). Phase separation of the LINE-1 ORF1 protein is mediated by the N-terminus and coiled-coil domain. Biophys. J. *120*, 2181–2191. https://doi.org/10.1016/j.bpj.2021.03.028.

54. Seim, I., Posey, A.E., Snead, W.T., Stormo, B.M., Klotsa, D., Pappu, R.V., and Gladfelter, A.S. (2022). Dilute phase oligomerization can oppose phase separation and modulate material properties of a ribonucleoprotein condensate. Proc. Natl. Acad. Sci. *119*, e2120799119. https://doi.org/10.1073/pnas.2120799119.

55. Hilditch, A.T., Romanyuk, A., Cross, S.J., Obexer, R., McManus, J.J., and Woolfson, D.N. (2024). Assembling membraneless organelles from de novo designed proteins. Nat. Chem. *16*, 89–97. https://doi.org/10.1038/s41557-023-01321-y.

56. Ramirez, D.A., Hough, L.E., and Shirts, M.R. (2024). Coiled-coil domains are sufficient to drive liquid-liquid phase separation in protein models. Biophys. J. *123*, 703–717. https://doi.org/10.1016/j.bpj.2024.02.007.

57. Heller, E., Kurup, N., and Zhuang, X. (2025). The membrane skeleton is constitutively remodeled in neurons by calcium signaling. Science *389*, eadn6712. https://doi.org/10.1126/science.adn6712.

58. Brangwynne, C.P., Eckmann, C.R., Courson, D.S., Rybarska, A., Hoege, C., Gharakhani, J., Jülicher, F., and Hyman, A.A. (2009). Germline P Granules Are Liquid Droplets That Localize by Controlled Dissolution/Condensation. Science *324*, 1729–1732. https://doi.org/10.1126/science.1172046.

59. Milovanovic, D., Wu, Y., Bian, X., and De Camilli, P. (2018). A liquid phase of synapsin and lipid vesicles. Science *361*, 604–607. https://doi.org/10.1126/science.aat5671.

60. Boke, E., Ruer, M., Wühr, M., Coughlin, M., Lemaitre, R., Gygi, S.P., Alberti, S., Drechsel, D., Hyman, A.A., and Mitchison, T.J. (2016). Amyloid-like Self-Assembly of a Cellular Compartment. Cell *166*, 637–650. https://doi.org/10.1016/j.cell.2016.06.051.

61. Bose, M., Lampe, M., Mahamid, J., and Ephrussi, A. (2022). Liquid-to-solid phase transition of oskar ribonucleoprotein granules is essential for their function in Drosophila embryonic development. Cell *185*, 1308–1324.e23. https://doi.org/10.1016/j.cell.2022.02.022.

62. Kato, M., Han, T.W., Xie, S., Shi, K., Du, X., Wu, L.C., Mirzaei, H., Goldsmith, E.J., Longgood, J., Pei, J., et al. (2012). Cell-free Formation of RNA Granules: Low Complexity Sequence Domains Form Dynamic Fibers within Hydrogels. Cell *149*, 753–767. https://doi.org/10.1016/j.cell.2012.04.017.

63. Patel, A., Lee, H.O., Jawerth, L., Maharana, S., Jahnel, M., Hein, M.Y., Stoynov, S., Mahamid, J., Saha, S., Franzmann, T.M., et al. (2015). A Liquid-to-Solid Phase Transition of the ALS Protein FUS Accelerated by Disease Mutation. Cell *162*, 1066–1077. https://doi.org/10.1016/j.cell.2015.07.047.

64. Cheng, X., and Case, L.B. (2025). Condensates control the actin cytoskeleton. Dev. Cell *60*, 1519–1520. https://doi.org/10.1016/j.devcel.2025.04.015.

65. Walker, C., Chandrasekaran, A., Mansour, D., Graham, K., Torres, A., Wang, L., Lafer, E.M., Rangamani, P., and Stachowiak, J.C. (2025). Liquid-like condensates that bind actin promote assembly and bundling of actin filaments. Dev. Cell *60*, 1550–1567.e4. https://doi.org/10.1016/j.devcel.2025.01.012.

66. Miyazaki, M., Chiba, M., Eguchi, H., Ohki, T., and Ishiwata, S. (2015). Cell-sized spherical confinement induces the spontaneous formation of contractile actomyosin rings in vitro. Nat. Cell Biol. *17*, 480–489. https://doi.org/10.1038/ncb3142.

67. Feng, Z., Caballe, A., Wainman, A., Johnson, S., Haensele, A.F.M., Cottee, M.A., Conduit, P.T., Lea, S.M., and Raff, J.W. (2017). Structural Basis for Mitotic Centrosome Assembly in Flies. Cell *169*, 1078–1089.e13. https://doi.org/10.1016/j.cell.2017.05.030.

68. Jiang, X., Ho, D.B.T., Mahe, K., Mia, J., Sepulveda, G., Antkowiak, M., Jiang, L., Yamada, S., and Jao, L.E. (2021). Condensation of pericentrin proteins in human cells illuminates phase separation in centrosome assembly. J. Cell Sci. *134*, jcs258897. https://doi.org/10.1242/jcs.258897.

69. Sahu, S., Chauhan, P., Lumen, E., Moody, K., Peddireddy, K., Mani, N., Subramanian, R., Robertson-Anderson, R., Wolfe, A.J., and Ross, J.L. (2023). Interplay of self-organization of microtubule asters and crosslinking protein condensates. PNAS Nexus *2*, pgad231. https://doi.org/10.1093/pnasnexus/pgad231.

70. Ramirez, D.A., Shrimpton, A., Shirts, M.R., and Hough, L.E. (2025). Nonspecific interactions can lead to liquid-liquid phase separation in coiled-coil proteins models. Preprint at bioRxiv. https://doi.org/10.1101/2025.05.09.653163.

71. Murakoshi, H., Lee, S.-J., and Yasuda, R. (2008). Highly sensitive and quantitative FRET–FLIM imaging in single dendritic spines using improved non-radiative YFP. Brain Cell Biol. *36*, 31–42.

72. Guardia, C.M., De Pace, R., Sen, A., Saric, A., Jarnik, M., Kolin, D.A., Kunwar, A., and Bonifacino, J.S. (2019). Reversible association with motor proteins (RAMP): A streptavidin-based method to manipulate organelle positioning. PLoS Biol. *17*, e3000279.

73. Patterson, G.H., and Lippincott-Schwartz, J. (2002). A photoactivatable GFP for selective photolabeling of proteins and cells. Science *297*, 1873–1877.

74. Choudhury, A., Dominguez, M., Puri, V., Sharma, D.K., Narita, K., Wheatley, C.L., Marks, D.L., and Pagano, R.E. (2002). Rab proteins mediate Golgi transport of caveola-internalized glycosphingolipids and correct lipid trafficking in Niemann-Pick C cells. J. Clin. Invest. *109*, 1541–1550.

75. Vonderheit, A., and Helenius, A. (2005). Rab7 associates with early endosomes to mediate sorting and transport of Semliki forest virus to late endosomes. PLoS Biol. *3*, e233.

76. Burkel, B.M., Von Dassow, G., and Bement, W.M. (2007). Versatile fluorescent probes for actin filaments based on the actin-binding domain of utrophin. Cell Motil. Cytoskelet. *64*, 822–832.

77. Gerrow, K., Romorini, S., Nabi, S.M., Colicos, M.A., Sala, C., and El-Husseini, A. (2006). A preformed complex of postsynaptic proteins is involved in excitatory synapse development. Neuron *49*, 547–562.

78. Campbell, B.C., Nabel, E.M., Murdock, M.H., Lao-Peregrin, C., Tsoulfas, P., Blackmore, M.G., Lee, F.S., Liston, C., Morishita, H., and Petsko, G.A. (2020). mGreenLantern: a bright monomeric fluorescent protein with rapid expression and cell filling properties for neuronal imaging. Proc. Natl. Acad. Sci. USA *117*, 30710–30721.

79. Gitler, D., Xu, Y., Kao, H.-T., Lin, D., Lim, S., Feng, J., Greengard, P., and Augustine, G.J. (2004). Molecular determinants of synapsin targeting to presynaptic terminals. J. Neurosci. *24*, 3711–3720.

80. Parra-Rivas, L.A., Madhivanan, K., Aulston, B.D., Wang, L., Prakashchand, D.D., Boyer, N.P., Saia-Cereda, V.M., Branes-Guerrero, K., Pizzo, D.P., and Bagchi, P. (2023). Serine-129 phosphorylation of α-synuclein is an activity-dependent trigger for physiologic protein-protein interactions and synaptic function. Neuron *111*, 4006–4023.e4010.

81. Schindelin, J., Arganda-Carreras, I., Frise, E., Kaynig, V., Longair, M., Pietzsch, T., Preibisch, S., Rueden, C., Saalfeld, S., and Schmid, B. (2012). Fiji: an open-source platform for biological-image analysis. Nat. Methods *9*, 676–682.

82. Ganguly, A., and Roy, S. (2014). Using Photoactivatable GFP to Track Axonal Transport Kinetics. Methods Mol. Biol. *1148*, 203–215. https://doi.org/10.1007/978-1-4939-0470-9_13.

83. Roy, S., Yang, G., Tang, Y., and Scott, D.A. (2011). A simple photoactivation and image analysis module for visualizing and analyzing axonal transport with high temporal resolution. Nat. Protoc. *7*, 62–68. https://doi.org/10.1038/nprot.2011.428.

84. Sharma, R., Gulia, R., and Bhattacharyya, S. (2019). Analysis of ubiquitination and ligand-dependent trafficking of group I mGluRs. Methods Cell Biol. *149*, 107–130. https://doi.org/10.1016/bs.mcb.2018.08.008.

85. Jimenez, A., Friedl, K., and Leterrier, C. (2020). About samples, giving examples: Optimized Single Molecule Localization Microscopy. Methods *174*, 100–114. https://doi.org/10.1016/j.ymeth.2019.05.008.

86. Ovesný, M., Křížek, P., Borkovec, J., Švindrych, Z., and Hagen, G.M. (2014). ThunderSTORM: a comprehensive ImageJ plug-in for PALM and STORM data analysis and super-resolution imaging. Bioinformatics *30*, 2389–2390. https://doi.org/10.1093/bioinformatics/btu202.

87. Friedl, K., Mau, A., Boroni-Rueda, F., Caorsi, V., Bourg, N., Lévêque-Fort, S., and Leterrier, C. (2023). Assessing crosstalk in simultaneous multicolor single-molecule localization microscopy. Cell Rep. Methods *3*, 100571. https://doi.org/10.1016/j.crmeth.2023.100571.

88. Bingham, D., Jakobs, C.E., Wernert, F., Boroni-Rueda, F., Jullien, N., Schentarra, E.M., Friedl, K., Da Costa Moura, J., van Bommel, D.M., Caillol, G., et al. (2023). Presynapses contain distinct actin nanostructures. J. Cell Biol. *222*, e202208110. https://doi.org/10.1083/jcb.202208110.

89. Li, Y., Shi, W., Liu, S., Cavka, I., Wu, Y.L., Matti, U., Wu, D., Koehler, S., and Ries, J. (2022). Global fitting for high-accuracy multi-channel single-molecule localization. Nat. Commun. *13*, 3133. https://doi.org/10.1038/s41467-022-30719-4.

90. Schindelin, J., Arganda-Carreras, I., Frise, E., Kaynig, V., Longair, M., Pietzsch, T., Preibisch, S., Rueden, C., Saalfeld, S., Schmid, B., et al. (2012). Fiji: an open-source platform for biological-image analysis. Nat. Methods *9*, 676–682. https://doi.org/10.1038/nmeth.2019.

91. Ganguly, A., Han, X., Das, U., Wang, L., Loi, J., Sun, J., Gitler, D., Caillol, G., Leterrier, C., Yates, J.R., 3rd, and Roy, S. (2017). Hsc70 chaperone activity is required for the cytosolic slow axonal transport of synapsin. J. Cell Biol. *216*, 2059–2074. https://doi.org/10.1083/jcb.201604028.

92. Scott, D.A., Das, U., Tang, Y., and Roy, S. (2011). Mechanistic Logic Underlying the Axonal Transport of Cytosolic Proteins. Neuron *70*, 441–454. https://doi.org/10.1016/j.neuron.2011.03.022.

93. Applewhite, D.A., Barzik, M., Kojima, S.I., Svitkina, T.M., Gertler, F.B., and Borisy, G.G. (2007). Ena/VASP proteins have an anti-capping independent function in filopodia formation. Mol. Biol. Cell *18*, 2579–2591. https://doi.org/10.1091/mbc.E06-11-0990.

94. Boyer, N.P., McCormick, L.E., Menon, S., Urbina, F.L., and Gupton, S.L. (2020). A pair of E3 ubiquitin ligases compete to regulate filopodial dynamics and axon guidance. J. Cell Biol. *219*, e201902088. https://doi.org/10.1083/jcb.201902088.

95. Ganguly, A., Sharma, R., Boyer, N.P., Wernert, F., Phan, S., Boassa, D., Parra, L., Das, U., Caillol, G., Han, X., et al. (2021). Clathrin packets move in slow axonal transport and deliver functional payloads to synapses. Neuron *109*, 2884–2901.e7. https://doi.org/10.1016/j.neuron.2021.08.016.

96. Mason, A.J. (2012). OpenSolver - An Open Source Add-in to Solve Linear and Integer Progammes in Excel. In Operations Research Proceedings 2011, D. Klatte, H.J. Lüthi, and K. Schmedders, eds. (Berlin, Heidelberg: Springer), pp. 401–406. https://doi.org/10.1007/978-3-642-29210-1_64.

97. Mészáros, B., Erdős, G., and Dosztányi, Z. (2018). IUPred2A: context-dependent prediction of protein disorder as a function of redox state and protein binding. Nucleic Acids Res. *46*, W329–W337. https://doi.org/10.1093/nar/gky384.

98. Erdős, G., and Dosztányi, Z. (2020). Analyzing Protein Disorder with IUPred2A. Curr. Protoc. Bioinforma. *70*. https://doi.org/10.1002/cpbi.99.

99. Oates, M.E., Romero, P., Ishida, T., Ghalwash, M., Mizianty, M.J., Xue, B., Dosztányi, Z., Uversky, V.N., Obradovic, Z., Kurgan, L., et al. (2013). D2P2: database of disordered protein predictions. Nucleic Acids Res. *41*, D508–D516. https://doi.org/10.1093/nar/gks1226.

STAR★METHODS

KEY RESOURCES TABLE

REAGENT or RESOURCE	SOURCE	IDENTIFIER
Antibodies		
Rabbit Polyclonal against Adducin1	Abcam	Cat#ab51130; RRID:AB_867519
Mouse monoclonal against αII-spectrin	Abcam	Cat#ab11755; RRID:AB_298540
Mouse monoclonal against βII-spectrin	BD Bioscience	Cat# 612563; RRID:AB_399854
Chicken polyclonal against βIII-tubulin	Abcam	Cat# ab41489; RRID:AB_727049
Chicken polyclonal against MAP2	Abcam	Cat# ab5392; RRID:AB_2138153
Rabbit polyclonal Anti-GFP	Abcam	Cat# ab290; RRID:AB_303395
Chicken monoclonal against mScarlet	Synaptic Systems	Cat#409006; RRID:AB_2725776
Goat anti-Chicken IgY (H+L) Secondary Antibody, Alexa Fluor^{TM} 647	Invitrogen	Cat#A21449; RRID:AB_2535866
Goat anti-Rabbit IgG (H+L) Cross-Adsorbed Secondary Antibody, Alexa Fluor^{TM} 594	Invitrogen	Cat# A11012; RRID:AB_2534079
Chicken antibody DyLight^{TM} 405	Rockland	Cat# 603-146-126; RRID:AB_1961602
Goat anti-Mouse IgG (H+L) Cross-Adsorbed Secondary Antibody, Alexa Fluor^{TM} 594	Invitrogen	Cat# A11005; RRID:AB_2534073
Goat anti-Rabbit IgG (H+L) Highly Cross-Adsorbed Secondary Antibody, Alexa Fluor^{TM} 647	Invitrogen	Cat# A21245; RRID:AB_2535813
Goat anti-Mouse IgG (H+L) Cross-Adsorbed Secondary Antibody, Alexa Fluor^{TM} 647	Invitrogen	Cat# A21235; RRID:AB_2535804
Goat anti-Rabbit IgG (H+L) Cross-Adsorbed Secondary Antibody, Alexa Fluor^{TM} 488	Invitrogen	Cat# A11008; RRID:AB_143165
Goat anti-Mouse IgG (H+L) Cross-Adsorbed Secondary Antibody, Alexa Fluor^{TM} 488	Invitrogen	Cat# A11001; RRID:AB_2534069
Chemicals, peptides, and recombinant proteins		
Dynasore	Abcam	Cat# ab120192
Alexa Fluor 488 conjugated phalloidin	Invitrogen	Cat# A12379
Alexa Fluor Plus 647–phalloidin	Invitrogen	Cat# A30107
Alexa Fluor 594 conjugated Deoxyribonuclease I	Invitrogen	Cat# D12372
Latrunculin A	Calbiochem	Cat# 428026
DMSO	Sigma-Aldrich	Cat# D2650
HBSS	GIBCO	Cat#14025092
Lipofectamine 2000	Life Technologies	Cat#11668-019
ProFection® Mammalian Transfection System	Promega	Cat#E1200
B27 supplement	GIBCO	Cat#17504044
Glutamax	GIBCO	Cat#35050061
Neurobasal A	GIBCO	Cat#10888022
poly-D-lysine	Sigma	Cat#P0899
Hibernate-E low fluorescence medium	Brainbits	Cat#HE-lf
0.25 % Trypsin–EDTA	Invitrogen	Cat#25200072
Fetal bovine serum	Hyclone	Cat#SH30071.03
Paraformaldehyde (16% aqueous solution)	Electron Microscopy Sciences	Cat#15710
Protease inhibitor cocktail	Sigma-Aldrich	Cat#P8340
dSTORM Super Resolution buffer	Abbelight	

(*Continued on next page*)

Continued

REAGENT or RESOURCE	SOURCE	IDENTIFIER
Experimental models: Organisms/strains		
Mouse: CD1	Charles River Laboratories	Cat#022-CD1
Recombinant DNA		
pCAG-mGFP-Actin	Murakoshi et al.[71]	Addgene Plasmid #21948
GFP-SBP-TOM20	Guardia et al.[72]	Addgene Plasmid #120173
FL- βII-spectrin:mGL	This paper	N/A
FL- αII-spectrin:mGL	This paper	N/A
FL- adducin:mGL	This paper	N/A
ΔSH3 - αII-spectrin:mGL	This paper	N/A
SR5-20 - αII-spectrin:mGL	This paper	N/A
SR8-10 - αII-spectrin:mGL	This paper	N/A
SR8-10 - αII-spectrin:mSc	This paper	N/A
SR1-9 - αII-spectrin:mGL	This paper	N/A
SR1-17 - βII-spectrin:mGL	This paper	N/A
SR1-17 - βII-spectrin:mSc	This paper	N/A
PH- βII-spectrin:mGL	This paper	N/A
ΔCH-CH- βII-spectrin:mGL	This paper	N/A
pPAGFP-C1	Patterson et al.[73]	Addgene plasmid #11910
IDR-PHD-IDR - βII-spectrin:mGL	This paper	N/A
full-length murine Adducin1	N/A	(Genbank NM_001024458)
Aldolase - adducin:mGL	This paper	N/A
NES-IDR - adducin:mGL	This paper	N/A
ΔIDR - adducin:mGL	This paper	N/A
ΔN-term - adducin:mGL	This paper	N/A
DsRed-Rab11 WT	Choudhury et al.[74]	Addgene Plasmid #12679
mRFP-Rab5	Vonderheit et al.[75]	Addgene Plasmid #14437
GFP-UtrCH	Burkel et al.[76]	Addgene Plasmid #26737
synaptophysin:mCh	Gerrow et al.[77]	N/A
pcDNA3.1-mGreenLantern	Campbell et al.[78]	Addgene Plasmid #161912
pcDNA_RGG-GFP-RGG	Schuster et al., 2018[31]	Addgene Plasmid #124939
mStayGold:SR1-17 βII-spectrin	This paper	N/A
GFP:synapsin-1a	Gitler et al.[79]	N/A
EGFP:βII-spectrin	Dr. Damaris Lorenzo, University of North Carolina	N/A
Actin-chromobody	Proteintech	Cat# acg
pCCL-mScarlet	LA Parra-Rivas et al.[80]	Addgene Plasmid #209889
pEGFP-N1	Clonetech	Cat#6085-1
Software and algorithms		
GraphPad Prism	GraphPad Software, La Jolla, CA, USA	Version 7.00; www.graphpad.com; RRID:SCR_002798
Fiji ImageJ	Schindelin et al.[81]	https://imagej.net/Fiji; RRID:SCR_002285
MetaMorph Version 7.10	Molecular Devices	https://www.moleculardevices.com/products/cellular-imaging-systems/acquisition-and-analysis-software/metamorph-microscopy; RRID:SCR_002368
Adobe Illustrator	Adobe	https://www.adobe.com/products/illustrator/free-trial-download.html; RRID:SCR_010279

(*Continued on next page*)

Continued

REAGENT or RESOURCE	SOURCE	IDENTIFIER
NIS Elements 5.30.05 software	Nikon	NIS-Elements | Software | Microscope Products | Nikon Instruments Inc. RRID:SCR_014329
ChriSTORM scripts	GitHub	http://github.com/cleterrier/ChriSTORM RRID:SCR_002427
ThunderSTORM scripts	GitHub	https://zitmen.github.io/thunderstorm/RRID:SCR_016897
N-STORM software	Nikon	https://www.microscope.healthcare.nikon.com/products/super-resolution-microscopes/n-storm-super-resolution; RRID:SCR_018302

EXPERIMENTAL MODEL AND SUBJECT DETAILS

Animals and cell-lines

Primary mouse hippocampal neuron cultures were prepared from CD1 pups (both sexes) obtained from Charles River Laboratories (Cat#022-CD1). Rat neuron cultures were produced by extracting hippocampi from E18 rat pups (both sexes) from pregnant female Wistar rats (Janvier labs). Brain tissues were collected from female C57BL/6J (8-10 weeks old) mice obtained from Jackson Laboratories. The influence of sex, gender, or both on the results is unknown. A separate study would be necessary to determine any sex-specific associations. Mycoplasma-free frozen stocks of validated HEK293T cells were obtained from ATCC and thawed to initiate cultures for experiments. All procedures were in agreement with the guidelines established by the University of California San Diego IACUC Office or the European Animal Care and Use Committee (86/609/CEE).

METHOD DETAILS

Plasmids, antibodies, and reagents

The pCAG-mGFP-Actin (#21948), GFP-SBP-Tom20 (#120173), DsRed-rab11 WT (#12679), mRFP-Rab5 (#14437), pcDNA3.1-mGreenLantern (#161912) and pcDNA_RGG-GFP-RGG (#124939) plasmids were acquired from Addgene. All mGreenLantern-tagged constructs consist of ORFs inserted into the multiple cloning site of pcDNA3.1-mGreenLantern using a Gibson cloning kit (NEBuilder HiFi DNA Assembly Cloning Kit, New England Biolabs). Intersectin($SH3_5$) was cloned from a construct generously gifted by the lab of Dr. Pietro De Camilli (Yale School of Medicine). Murine βII-spectrin and human αII-spectrin constructs were cloned from templates generously gifted by the lab of Dr. Matthew Rasband (Baylor College of Medicine), and fluorescent tags were inserted into the C-terminus of spectrin (previous studies have shown C-terminally tagged bII-spectrin can incorporate into the MPS[21]). βII-spectrin full-length, ΔCH_2 (aa303-2363) and SR1-17 (aa303-2084), and αII-spectrin SR8-10 (aa783-1242) and SR1-9 (aa1-969) inserts were generated by PCR from templates. αII-spectrin full length protein, ΔSH3 (aa967-1026 replaced with GGGG), and SR5-20 (aa468-2310) constructs were generated from these templates by a commercial cloning service (VectorBuilder Inc.). Inserts for βII-spectrin IDR-PHD-IDR (aa2085-2363), full-length murine Adducin1 (Genbank NM_001024458), Adducin1 aldolase (aa141-332) and NES-IDR (aa377-391 fused to aa544-735) were generated by custom oligonucleotide synthesis (gBlocks Gene Synthesis, Integrated DNA Technologies, Inc.). Adducin1 ΔIDR (aa1-577) and ΔN-term (aa141-735) inserts were cloned from Adducin1:mGreenLantern by PCR. Scarlet-tagged constructs were created by Gibson assembly of inserts generated by PCR from βII-spectrin SR1-17:mGreenLantern and αII-spectrin SR8-10:mGreenLantern inserted into pCCL-mScarlet (Addgene, #209889). The mStayGold:SR1-17 βII-spectrin fragment was generated from a full-length EGFP:βII-spectrin sequence (gift from Dr. Damaris Lorenzo, University of North Carolina). Actin-chromobody was purchased from Proteintech (Cat# acg).

Primary antibodies used in this study: rabbit polyclonal against Adducin1 (Abcam ab51130), mouse monoclonal against αII-spectrin (Abcam ab11755), mouse monoclonal against βII-spectrin (BD Bioscience #612563), chicken polyclonal against βIII-tubulin (Abcam ab41489), chicken polyclonal against MAP2 (Abcam ab-5392), rabbit polyclonal Anti-GFP antibody (Abcam ab-290) and chicken monoclonal against mScarlet (Synaptic systems #409006). Secondary antibodies used in this study: goat anti-chicken Alexa Fluor 647 conjugate (Invitrogen A21449), goat anti-rabbit Alexa Fluor 594 conjugate (Invitrogen A11012), chicken antibody DyLight™ 405 (Rockland Cat# 603-146-126), goat anti-mouse Alexa Fluor 594 conjugate (Invitrogen A11005), goat anti-rabbit Alexa Fluor 647 conjugate (Invitrogen A21245), goat anti-mouse Alexa Fluor 647 conjugate (Invitrogen A21235), goat anti-rabbit Alexa Fluor 488 conjugate (Invitrogen A11008) and goat anti-mouse Alexa Fluor 488 conjugate (Invitrogen A11001). Additional reagents used in these studies: Alexa Fluor 488 conjugated phalloidin (Invitrogen A12379), Alexa Fluor 594 conjugated Deoxyribonuclease I (Invitrogen D12372), Latrunculin A (Calbiochem #428026), and DMSO (Sigma-Aldrich D2650).

Neuronal cultures, transfections, and immunocytochemistry

Mouse hippocampal neurons were obtained from brains of postnatal (P0) CD-1 mice and plated on Cellvis glass-bottom dishes as described previously,[82,83] in compliance with University of California guidelines. Briefly, Cellvis dishes were coated with 100μL of 1 mg/mL poly-D-lysine + 1 mg/mL mouse laminin overnight at room temperature, washed thrice with ddH_2O, and air-dried before plating. Hippocampi from P0 pups were dissected in ice-cold dissection buffer (HBSS, 4.44 mM D-glucose, and 6.98 mM HEPES) and incubated in 0.25% Trypsin-EDTA at 37°C for 15 minutes. Neurons were then dissociated in plating media (90% Neurobasal/B27 + 10% FBS, Life Technologies) by trituration. Neurons were plated at a density of 3,000 cells/100μL (immunostaining assays) or 30,000 cells/100μL (FRAP assays) of plating media. Neurons were maintained in NB27 media (Neurobasal media supplemented with 2% B27 and 1% GlutaMAX) in an incubator at 37°C and 5% CO_2.

Rat hippocampal neurons were obtained from E18 rat pups from pregnant female Wistar rats. Hippocampi were dissected and homogenized by trypsin treatment followed by mechanical trituration and seeded on 18-mm diameter round, #1.5H coverslips at a density of 12,000-20,000 cells/cm^2 for 3 hours in serum-containing plating medium (MEM with 10% fetal bovine serum, 0.6% added glucose, 0.08 mg/mL sodium pyruvate, 100 UI/mL penicillin-streptomycin). Coverslips were then transferred, cells down, to petri dishes containing confluent glia cultures conditioned in NB27+ medium (Neurobasal medium supplemented with 2% B-27, 100UI/mL penicillin/streptomycin and 2.5 μg/mL amphotericin) and cultured in these dishes (Banker method[67]). Neurons were transfected with the designated fluorescent constructs (1 μg of DNA) at 3-7 DIV. Transfection was carried out using either Lipofectamine 2000 from Life Technologies or a calcium phosphate transfection kit from Promega.[84] For immunostaining, neurons were fixed in 4% paraformaldehyde in PEMS (80 mM PIPES, 5 mM EGTA, 2 mM $MgCl_2$, 4% sucrose, pH 6.8) for 15 min at room temperature, followed by 3 rinses in 1X PBS. Cells were permeabilized in 0.2% Triton X-100 for 10 min, and blocked in 1X PBS containing 10% bovine serum albumin for 2 hours at room temperature. Neurons were incubated overnight at 4°C with primary antibodies in blocking buffer, washed three times with 1X PBS, then incubated with secondary antibodies labeled with Alexa Fluor fluorophores for 1 hour at room temperature. Cells were washed three times with 1X PBS and then mounted with Fluoro-Gel mounting media (Electron Microscopy Sciences #50-247-04). Immunostained neurons were imaged on a Nikon Eclipse Ti-E inverted epifluorescence microscope equipped with CFI Plan Apochromat VC 100X oil (NA 1.4; Nikon) objective, and an electron-multiplying charge-coupled device camera (QuantEM:512SC; Photometrics).

Tissue processing and immunofluorescence staining

C57BL/6J (Jackson Labs) mice were euthanized by CO2 asphyxiation and decapitation. Brains were extracted and drop-fixed in 4% PFA for at least 24 hours before paraffin embedding. Embedded tissues were sectioned at 5μm on a microtome and mounted on Superfrost Plus glass slides (Fisher, 22-037-246). Tissues were deparaffinized for 15 minutes in Citrisolve and rehydrated in ethanol and TBS before antigen retrieval was performed using a citrate antigen unmasking solution (Vector Labs, H-3300-250) for 25 min at 100°C in an InstantPot pressure cooker. Slides were subsequently blocked 45 min RT in 5% Normal Donkey Serum, 0.1% Triton-X-100 in TBS. Primary antibodies were diluted in blocking solution (αII-spectrin, Abcam ab11755, 1:1000; βIII-tubulin Abcam ab52623, 1:2000) and slides were incubated 16hrs 4°C. After washing, slides were incubated in Alexa fluor conjugated secondary antibodies (Jackson ImmunoResearch, 1:200, 45min, RT). Slides were washed a final time and mounted on coverslips with Fluoromount G with DAPI mounting medium. After curing for 24hrs, slides were imaged on an Olympus VS200 slide scanner at 20x and 40x magnification.

Discontinuity factor

The discontinuity factor was calculated from fluorescence linescans of full axons. This factor at a given point *x* along the axon was defined as the difference between the maximum and minimum fluorescence within 5 microns of *x*, normalized to the median fluorescence within 20 microns. This is expressed as the equation:

$$\delta(x) = \log\left(\frac{\max\limits_{x\pm 5\mu m}\left(\boldsymbol{M}_{1\mu m}\right) - \min\limits_{x\pm 5\mu m}\left(\boldsymbol{M}_{1\mu m}\right)}{\boldsymbol{M}_{20\mu m}}\right)$$

where $\boldsymbol{M}_{1\mu m}$ and $\boldsymbol{M}_{20\mu m}$ are the 1μm and 20μm micron moving medians, respectively. The 1 micron moving median was used to reduce the impact of visual noise on measurements. A logarithm was applied to the value in order to reduce edge effects from the increased intensity of the soma and growth cone.

STORM super-resolution microscopy

Rat hippocampal neurons from E18 embryos were cultured on 18 mm coverslips at a density of 6,000/cm^2 following guidelines established by the European Animal Care and Use Committee (86/609/CEE) and approval of the local ethics committee (agreement D13-055-8). After 6 DIV, neurons were fixed, processed and imaged as previously described.[2,85] Neurons were fixed with 4% glutaraldehyde, 4% sucrose in PEM buffer (80mM PIPES pH 6.8, 5mM EGTA, 2mM $MgCl_2$) for 10 minutes at room temperature, blocked in blocking buffer (phosphate buffer 0.1M with 0.22% gelatin, 0.1% Triton X-100) for 2h, stained with primary antibodies overnight, and then secondary antibodies for 1h in blocking buffer, followed if needed with incubation with phalloidin coupled to Alexa Fluor Plus 647 (Thermo Fischer Scientific #A30107). For imaging, coverslips were placed in STORM buffer

(Abbelight). For single-color STORM, samples were imaged on an N-STORM microscope (Nikon Instruments). A series of 60,000 images (67Hz frame rate) was acquired at full power with a 647nm laser, with progressive reactivation with a 405nm laser. Sequences of images were processed for localizations using the N-STORM software and 2D projections of the 3D-STORM data were generated using the ThunderSTORM plugin for ImageJ[86] and the ChriSTORM scripts (https://github.com/cleterrier/ChriSTORM). For two-color STORM, a SAFe360 module (Abbelight) mounted on an inverted Nikon Ti2 stand (Nikon) was used to perform spectral-demixing STORM[87] of actin labeled with phalloidin Alexa Fluor Plus 647 and αII/βII-spectrin labeled using a CF680-conjugated antibody as described previously.[88] Localization and image processing was performed using GlobLoc[89] with final rendering using ThunderSTORM and ChriSTORM.

SIM super-resolution microscopy

A Nikon-SIM S microscope was used to acquire SIM images at two distinct locations along the axon of transfected rat neurons: proximal axon (around ~100 μm from the cell body) and distal axon (~200-300 μm from the cell body). Exposure times and laser powers were: 488nm, ~200 msec at ~80 percent laser power; 561 nm, ~100 msec at ~30 percent laser power. The objective was a CFI Apochromat TIRF 100XC Oil (NA 1.49) objective and the system was equipped with a TI2-FT N-SIM 405/488/561/640 quad band filter cube and corresponding emission filters. Images were acquired in 3D-SIM mode (15 raw images per frame) as Z-stacks with a spacing of 0.12 μm. The microscope used an ORCA-Fusion BT camera (Hamamatsu Photonics K.K. – C15440-20UP) and was controlled by NIS Elements 5.30.05 software. Reconstruction was performed using the N-SIM module within NIS-Elements. The acquired image pixel size was 0.065 μm and the final pixel size of processed SIM images was 0.032 μm, with an XYZ resolution of ~120 x 120 x 240 nm.

SIM image analysis

A set of macros (adapted from https://github.com/cleterrier/Process_Images) within Fiji[90] was used to process the reconstructed SIM images. In brief, nd2 Z-stacks are initially extracted to tif files, then projected along Z using a maximum projection and all images from a given experiment are grouped as a hyperstack that was used for the analysis of axonal periodicity. A set of macros (adapted from https://github.com/cleterrier/Measure_ROIs) was used to classify periodic regions along axonal segments. Axons were manually traced along their whole length using the ‘segmented lines’ tool (line width of 10 pixels), and the visibly periodic segments along the axons were traced separately. The length of the “whole” and “periodic” line ROIs was then measured and used to calculate the % periodicity along axons for the different locations (proximal, distal) and conditions.

Live-cell spinning-disk imaging

Live-cell imaging of mStayGold:SR(1-17) expressing rat neurons was performed on a Yokogawa CSU-W1 spinning disk microscope equipped with a SoRa pixel reassignment module, a Ti2-E stand (Nikon), a 60X NA 1.49 oil objective, and a Fusion BT sCMOS camera (Hamamatsu) in live-cell imaging medium (Hibernate E low fluorescence, Brainbits/Thermo Fisher Scientific #NC0285514) supplemented with 3% glucose, 2% B27, and 0.5mM L-glutamine). Images of neurons expressing different levels of mStayGold:SR(1-17) were obtained using 488-nm laser excitation with identical power and camera exposure times and the mean intensity over the cell body area was quantified in Fiji.

Axonal FRAP

Neurons were transfected with the indicated fluorescent constructs at 5DIV with Lipofectamine 2000 (Invitrogen). At 7DIV, neurons were transferred to Hibernate media (Brainbits) supplemented with 2% B27, 2mM GlutaMAX, 0.4% D-glucose, 37.5 mM NaCl (HELF[83,91,92]) and maintained at 37°C for the duration of experiments (heated stage chamber, model STEV; World Precision Instrument, Inc.). Cells were imaged on the microscope described in Immunostaining section, which was also equipped with an Andor Mosaic3 Digital Micromirror Device (DMD) attached to a 405nm diode laser (450mW). Axons were identified by morphology, and only neurons with unambiguous morphology were selected for imaging.[83,92] Following previously published criteria for abnormal overexpressors (see Zhong et al. 2014[21]; Figure S2A) axons with rapid fluorescence recovery in the proximal region – indicating abnormal spectrin overexpression – were excluded from further analysis. Axonal segments of 1 μm length or full spectrin patches were bleached using the 405nm laser with 5 consecutive pulses of 1s each and imaged every 2 seconds for several minutes.

Droplet FRAP

HEK293T cells were maintained in DMEM + GlutaMAX supplemented with 10% FBS and 1% penicillin-streptomycin. Cultures were transfected using Lipofectamine 2000 (Invitrogen) 18-20 hours prior to imaging in HELF media. Cells were imaged on a Leica DMi8 inverted confocal microscope equipped with a 100x oil-immersion objective, live cell imaging chamber, and white light laser for photobleaching. Droplets were imaged at 14.3fps (RGG-GFP-RGG), 8.33fps (βII-spectrin SR1-17; αII-spectrin full length protein + SR8-10; αII-spectrin full length protein + βII-spectrin SR1-17), 1.15fps (Adducin ΔN-term), or 4.4fps (all other constructs). For all FRAP experiments, droplets were imaged for 3 frames, bleached for one frame using 100% laser power at 405nm and 488nm, and then imaged for 600 frames. Bleaching regions were drawn individually for each droplet and either encompassed the entire droplet (full-droplet FRAP) or approximately 50% of the droplet area (partial droplet FRAP).

QUANTIFICATION AND STATISTICAL ANALYSIS

FRAP quantification and other analyses

Full droplet and axonal FRAP data were analyzed as previously described.[93–95] Background fluorescence values were subtracted from data at each time point, and photobleaching was corrected by normalizing data to an unbleached control region in the same image. Fluorescence curves were normalized between cells by subtracting the fluorescence immediately after bleaching (time = 0), and then dividing by the average of the 3-5 pre-bleach fluorescence time points. Fluorescence recovery rate and mobile fraction were calculated from an inverse exponential decay ($F(t) = A * (1 - e^{-\tau t})$, where F is fluorescence, A is the recovery plateau fluorescence, τ is the recovery time constant, and t is time) fit to the fluorescence recovery curve for each droplet. Fluorescence recovery curves were fit to the data with the OpenSolver add-in of Microsoft Excel 2013[96] using the NOMAD non-linear formula algorithm.

Partial droplet FRAP dip depth was calculated from the average of the lowest 10 data points in the unbleached half, excluding the first 5 frames after bleach. The internal diffusion rate (D) was determined as described previously.[33] We calculated the recovery curve within the droplet (F_{diff}) as the difference between the recovery of the bleached half (F_{half}), which relies on diffusion within the droplet and flux at the condensate boundary, and the recovery of the full droplet (F_{full}), which only relies on boundary flux:

$$F_{\text{diff}}(t) = F_{\text{half}}(t) - F_{\text{full}}(t)$$

We then fit this curve to a simple diffusion model:

$$F_{\text{diff}}(t) = Ae^{-\frac{2\tau_D}{t}}\left[I_0(2\tau_D / t) + I_1(2\tau_D / t)\right]$$

where I_0 and I_1 are modified Bessel functions of the 0th and 1st order, respectively, and $\tau_D = R^2/(4D)$, with R defined as the radius of the bleached region and D the internal diffusion coefficient. For quantifying size and other parameters of axonal patches from images, a line scan profile of αII-spectrin patches on the axon was used to assess their size, spacing, and density. The length of the axon was represented on the x-axis, with the size of each patch determined by the width of the corresponding intensity peak. Spacing between peaks was designated as gaps. Colocalization of actin and αII-spectrin patches was quantified by counting the number of αII-spectrin patches that coincided with peaks of actin.

Protein disorder prediction

Protein disorder was predicted using the IUPred2A algorithm[97,98] and cross-referenced with the D2P2 protein disorder prediction database, which aggregates disorder predictions from several additional algorithms.[99] A region was considered to be disordered if it scored above 0.5 according to IUPred2A and met consensus with at least seven of the nine predictors included in the D2P2 database. The protein sequences used for prediction were murine αII-spectrin (Sptan1, P16546-1), murine βII-spectrin (Sptbn1, Q62261-1), and murine α-adducin (Add1, Q9QYC0-1).

Statistical analysis

Statistical tests were performed using GraphPad Prism. Normality of data sets was tested using the Shapiro-Wilk W test with α set at 0.05. Pairwise comparisons were made using a Student's t test when both groups compared were found to be normally distributed: in other cases, a Mann-Whitney nonparametric U test was used. When more than two groups were compared, a one-way ANOVA or Kruskal-Wallis test was used in the case of normally or non-normally distributed data, respectively, with Dunn's post-hoc pairwise comparisons against control groups when multiple comparison p was less than 0.05. Axonal FRAP curves were compared by two-way ANOVA interaction factor between time after bleach and condition. Actin colocalization with spectrin was compared between groups by two-way ANOVA interaction factor between axon segment and actin-containing fraction, with correction for multiple comparisons using the Bonferroni method. No *pre-hoc* sample size estimates were determined prior to experiments due to a lack of information on expected effect sizes. All data are presented as mean ± SEM. In all figures, significance is represented as follows: n.s., $p > 0.05$; *, $p < 0.05$; **, $p < 0.01$; ***, $p < 0.001$.